

Joint Center for Satellite Data Assimilation

Office Note (unassigned)

THIS IS AN UNREVIEWED MANUSCRIPT, PRIMARILY INTENDED FOR INFORMAL
EXCHANGE OF INFORMATION AMONG JCSDA RESEARCHERS

CRTM: Implementation of the Low Frequency Microwave Sea Surface Emissivity Model

Paul van Delst^a
JCSDA/EMC/SAIC

July, 2008

^apaul.vandelst@noaa.gov

Abstract

Implementing the low frequency microwave sea surface emissivity model of [Kazumori et al. \[2008\]](#) in the CRTM involved extensive refactoring of the code and subsequent tests of the consistency of the forward, tangent-linear and adjoint model. The code to compute the ocean surface permittivities according to the [Guillou et al. \[1998\]](#) model were also tested separately, as were the Fresnel reflectivity codes.

Fastem3 was implemented for instrument frequencies greater than 20GHz. Some initial CRTM comparisons were performed comparing the updated model with the current CRTM sea surface emissivity model, Fastem1.

Keywords: CRTM, low frequency microwave sea surface emissivity, Fastem3, Guillou permittivity, Fresnel reflectivity, forward, tangent-linear, adjoint model.

1 Introduction

This article documents the implementation and testing of a low-frequency microwave sea surface emissivity model in the CRTM. The model was developed for use with AMSR-E data, but is applicable to any frequencies below 20GHz. Characteristics of the model affecting the testing will be described, but for a full model description readers are referred to [Kazumori et al. \[2008\]](#). For frequencies greater than 20GHz, the Fastem3 model was implemented.

1.1 Model description

A flowchart of the forward model is shown in figure [1.1](#). The flowchart members outlined in red - the permittivity and reflectivity computations - were tested individually from the model and those results are discussed separately. This model is referred to as a low-frequency model since it is not invoked in the calling CRTM SfcOptics module unless the microwave channel frequency is less than 20GHz. For frequencies greater than 20GHz, the Fastem3 model (REF!) is called. Note however that the 20GHz branch is also performed in the model itself.

Additionally, note that for low frequencies the Guillou permittivity model [[Guillou et al., 1998](#)] is called. For frequencies greater than the 20GHz limit the Ellison permittivity model [[Ellison et al., 2003](#)] is called. One difference in the implementation of the Ellison model compared to its reference is that no salinity dependence was included. This is due to the model always being invoked for frequencies beyond 20GHz where the salinity dependence is negligible (or, at least, less than the precision of the measurements used to derive the relationships.)

Since this model is not called from the CRTM SfcOptics calling routine unless the frequency is $\leq 20\text{GHz}$, the Ellison permittivity model tests will not be shown. Only the Guillou permittivity model tests will be discussed.

With regards to the model flowchart of figure [1.1](#), note in particular the branch conditions for computing foam coverage at a wind speed of 7m.s^{-1} and for applying the small-scale correction to the Fresnel reflectivities at a frequency of 15GHz.

1.1.1 Small-scale correction to reflectivities

The reflectivities of the ocean surface are modified to account for the diffraction effect of small scale waves as described by [Guissard and Sobieski \[1987\]](#) (see eqn.5 in [Kazumori et al. \[2008\]](#)),

$$r_p = \begin{cases} r_{p,\text{Fresnel}} & : f \leq 15\text{GHz} \\ r_{p,\text{Fresnel}} \exp(-4k^2\zeta_R^2 \cos^2 \theta) & : f > 15\text{GHz} \end{cases} \quad (1.1)$$

where p designates either vertical or horizontal polarisation, θ is the incidence angle, k is the wavenumber of the radiation, and ζ_R is the ocean height variance. The value of ζ_R^2 is determined from the ocean wave spectrum as described in [Bjerkaas and Riedel \[1979\]](#). Note that the quantity $4k^2\zeta_R^2$ is precomputed as a function of both frequency and wind speed and stored as a look-up-table (LUT) in the source code.

1.1.2 Foam-coverage correction to reflectivities

Similarly, the reflectivity of the ocean surface considering foam is dealt with in [Kazumori et al. \[2008\]](#) (see eqn.20) by determining a foam coverage fraction and using that in a weighted average of the foam and foam-free reflectivities,

$$r_p = \begin{cases} r_{p,no-foam} & : v < 7.0\text{ms}^{-1} \\ a.r_{p,foam} + (1-a).r_{p,no-foam} & : v \geq 7.0\text{ms}^{-1} \end{cases} \quad (1.2)$$

where a is the computed foam coverage fraction¹.

¹[Kazumori et al. \[2008\]](#) uses the symbol f for foam coverage fraction. In this document, f is used to refer to frequencies.

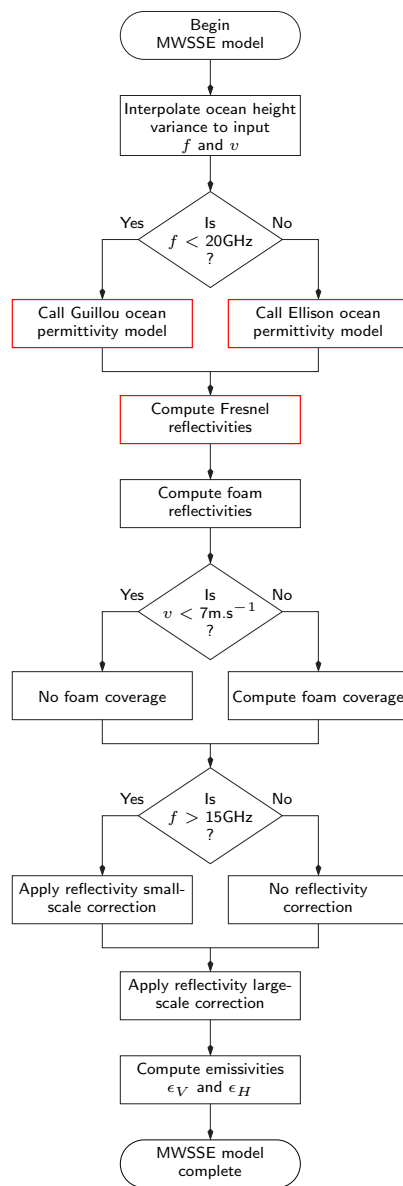


Figure 1.1: Flowchart of the forward microwave sea surface emissivity model. f and v are input frequency and wind speed respectively.

1.2 Test descriptions

Apart from comparisons with baseline results to ensure any code refactoring did not break anything, separate tests were performed to verify consistency between the forward and tangent-linear models, and the tangent-linear and adjoint models.

Regarding nomenclature: $F()$, $TL()$ and $AD()$ represent the forward, tangent-linear, and adjoint functions respectively; δx and δ^*x represent the tangent-linear and adjoint forms of a forward variable, x ; $\Re\{z\}$ and $\Im\{z\}$ represent the real and imaginary parts of a complex variable, z .

1.2.1 Forward/Tangent-Linear Test

The forward/tangent-linear (FWD/TL) test performed is,

$$\left| \frac{F(x + \alpha\delta x) - F(x - \alpha\delta x)}{2\alpha} - TL(\delta x) \right| < t_r \quad (1.3)$$

for $\delta x = 0.1$ and $\alpha = 0.1, 0.01, 0.001$, and 0.0001 . The value of a threshold residual value, t_r , is dependent on the test being performed and will be discussed further in the test result sections. For complex valued quantities, the tests were performed individually on the real and imaginary parts,

$$\left. \begin{aligned} & \left| \frac{\Re\{F(x + \alpha\delta x)\} - \Re\{F(x - \alpha\delta x)\}}{2\alpha} - \Re\{TL(\delta x)\} \right| \\ & \left| \frac{\Im\{F(x + \alpha\delta x)\} - \Im\{F(x - \alpha\delta x)\}}{2\alpha} - \Im\{TL(\delta x)\} \right| \end{aligned} \right\} < t_r \quad (1.4)$$

1.2.2 Tangent-Linear/Adjoint Test

The tangent-linear (TL/AD) test performed is,

$$\mathbf{TL}^T \mathbf{TL} = \delta \mathbf{x}^T \mathbf{AD}(TL) \quad (1.5)$$

where the input to the adjoint model is the output of the tangent-linear model for an input δx . A successful test occurs when the relationship shown in equation 1.5 is satisfied to within numerical precision.

For the main procedures that have real valued input (x_1, x_2, \dots) and real valued output (y_1, y_2, \dots), equation 1.5 uses

$$\begin{aligned} \mathbf{TL}^T \mathbf{TL} &\equiv \sum_i \delta y_i^2 \\ \delta \mathbf{x}^T \mathbf{AD}(TL) &\equiv \sum_i \delta x_i \cdot \delta^* x_i \end{aligned}$$

For procedures that have real valued input (x_1, x_2, \dots) and complex valued output (z), such as the permittivity routines, equation 1.5 uses

$$\begin{aligned} \mathbf{TL}^T \mathbf{TL} &\equiv \Re\{\delta z\}^2 + \Im\{\delta z\}^2 \\ \delta \mathbf{x}^T \mathbf{AD}(TL) &\equiv \sum_i \delta x_i \cdot \delta^* x_i \end{aligned}$$

For procedures that have complex valued input (z) and real valued output (y_1, y_2, \dots), such as the reflectivity routines, equation 1.5 uses

$$\begin{aligned} \mathbf{TL}^T \mathbf{TL} &\equiv \sum_i \delta y_i^2 \\ \delta \mathbf{x}^T \mathbf{AD}(TL) &\equiv \Re\{\delta z\}\Re\{\delta^* z\} + \Im\{\delta z\}\Im\{\delta^* z\} \end{aligned}$$

2 Interface Description

The model is called from the `Compute_MW_SfcOptics()` functions in the `CRTM_MW_Water_SfcOptics` module. The main source module is `CRTM_LowFrequency_MWSSEM` and it contains the public entities shown in table 2.1. Note that the internal variable structure is usable but not accessible outside the `CRTM_LowFrequency_MWSSEM` module.

Name	Description
Data types	
<code>iVar_type</code>	Internal variable struture
Subroutines	
<code>LowFrequency_MWSSEM</code>	Forward model
<code>LowFrequency_MWSSEM_TL</code>	Tangent-linear model
<code>LowFrequency_MWSSEM_AD</code>	Adjoint model

Table 2.1: List of public procedures in the `CRTM_LowFrequency_MWSSEM` module

The interface and argument descriptions for the forward model are shown in figure 2.1.

The interface and argument descriptions for the tangent-linear model are shown in figure 2.2. Note that the “internal variable” argument, `iVar`, is now an input as this structure contains intermediate forward model variables computed within the forward model. Also note that there are no frequency and zenith angle tangent-linear inputs. This model does not compute sensitivities of the emissivity to those quantities.

The interface and argument descriptions for the adjoint model are shown in figure 2.3. As with the tangent-linear interface, the internal variable argument, `iVar`, is an input. Note that if an argument is an input in the tangent-linear model, its corresponding adjoint argument is an output. Similarly, adjoint input arguments correspond with forward model output arguments. Note that although the adjoint emissivity is an input to the model, upon exiting the adjoint subroutine it is set to zero.

The temperature, salinity, and wind speed adjoints are all summed over the number of Stokes vector components as shown below,

$$\begin{aligned} \text{Temperature_AD} &= \sum_i^N \frac{\partial e_i}{\partial T} \\ \text{Salinity_AD} &= \sum_i^N \frac{\partial e_i}{\partial S} \\ \text{Wind_Speed_AD} &= \sum_i^N \frac{\partial e_i}{\partial W} \end{aligned}$$

where N is the number of Stokes vector components. Currently, this is fixed at 2 (vertical and horizontal polarisations only).

```

SUBROUTINE LowFrequency_MWSSEM( Frequency , & ! Input
                                Zenith_Angle, & ! Input
                                Temperature , & ! Input
                                Salinity , & ! Input
                                Wind_Speed , & ! Input
                                Emissivity , & ! Output
                                iVar ) ! Internal variable output
REAL(fp),      INTENT(IN)    :: Frequency
REAL(fp),      INTENT(IN)    :: Zenith_Angle
REAL(fp),      INTENT(IN)    :: Temperature
REAL(fp),      INTENT(IN)    :: Salinity
REAL(fp),      INTENT(IN)    :: Wind_Speed
REAL(fp),      INTENT(OUT)   :: Emissivity(:)
TYPE(iVar_type), INTENT(IN OUT) :: iVar

```

Argument	Description	Units	Intent
Frequency	Microwave frequency	GHz	IN
Zenith_Angle	Satellite zenith angle at the sea surface	Degrees	IN
Temperature	Sea surface temperature	Kelvin	IN
Salinity	Salinity of sea water	% _o	IN
Wind_Speed	Sea surface wind speed	m.s ⁻¹	IN
Emissivity	The surface emissivity at vertical and horizontal polarizations	N/A	OUT
iVar	Structure containing internal variables required for subsequent tangent-linear or adjoint model calls.	N/A	OUT

Figure 2.1: Forward model interface and argument description for the low frequency microwave sea surface emissivity model.

```

SUBROUTINE LowFrequency_MWSSEM_TL( Frequency      , & ! Input
                                    Zenith_Angle , & ! Input
                                    Temperature   , & ! FWD Input
                                    Salinity     , & ! FWD Input
                                    Wind_Speed   , & ! FWD Input
                                    Temperature_TL, & ! TL Input
                                    Salinity_TL  , & ! TL Input
                                    Wind_Speed_TL, & ! TL Input
                                    Emissivity_TL, & ! TL Output
                                    iVar          ) ! Internal variable input
REAL(fp),      INTENT(IN) :: Frequency
REAL(fp),      INTENT(IN) :: Zenith_Angle
REAL(fp),      INTENT(IN) :: Temperature
REAL(fp),      INTENT(IN) :: Salinity
REAL(fp),      INTENT(IN) :: Wind_Speed
REAL(fp),      INTENT(IN) :: Temperature_TL
REAL(fp),      INTENT(IN) :: Salinity_TL
REAL(fp),      INTENT(IN) :: Wind_Speed_TL
REAL(fp),      INTENT(OUT) :: Emissivity_TL(:)
TYPE(iVar_type), INTENT(IN) :: iVar

```

Argument	Description	Units	Intent
Frequency	Microwave frequency	GHz	IN
Zenith_Angle	Satellite zenith angle at the sea surface	Degrees	IN
Temperature	Sea surface temperature	Kelvin	IN
Salinity	Salinity of sea water	% _o	IN
Wind_Speed	Sea surface wind speed	m.s ⁻¹	IN
Temperature_TL	Sea surface temperature perturbation	Kelvin	IN
Salinity_TL	Salinity of sea water perturbation	% _o	IN
Wind_Speed_TL	Sea surface wind speed perturbation	m.s ⁻¹	IN
Emissivity_TL	The surface emissivity perturbation at vertical and horizontal polarizations	N/A	OUT
iVar	Structure containing internal variables. Output from the forward model.	N/A	IN

Figure 2.2: Tangent-linear model interface and argument description for the low frequency microwave sea surface emissivity model.

```

SUBROUTINE LowFrequency_MWSSEM_AD( Frequency      , & ! Input
                                    Zenith_Angle , & ! Input
                                    Temperature   , & ! FWD Input
                                    Salinity     , & ! FWD Input
                                    Wind_Speed   , & ! FWD Input
                                    Emissivity_AD , & ! AD Input
                                    Temperature_AD, & ! AD Output
                                    Salinity_AD   , & ! AD Output
                                    Wind_Speed_AD , & ! AD Output
                                    iVar          ) ! Internal variable input
REAL(fp),      INTENT(IN)      :: Frequency
REAL(fp),      INTENT(IN)      :: Zenith_Angle
REAL(fp),      INTENT(IN)      :: Temperature
REAL(fp),      INTENT(IN)      :: Salinity
REAL(fp),      INTENT(IN)      :: Wind_Speed
REAL(fp),      INTENT(IN OUT)  :: Emissivity_AD(:)
REAL(fp),      INTENT(IN OUT)  :: Temperature_AD
REAL(fp),      INTENT(IN OUT)  :: Salinity_AD
REAL(fp),      INTENT(IN OUT)  :: Wind_Speed_AD
TYPE(iVar_type), INTENT(IN)    :: iVar

```

Argument	Description	Units	Intent
Frequency	Microwave frequency	GHz	IN
Zenith_Angle	Satellite zenith angle at the sea surface	Degrees	IN
Temperature	Sea surface temperature	Kelvin	IN
Salinity	Salinity of sea water	% _o	IN
Wind_Speed	Sea surface wind speed	m.s ⁻¹	IN
Emissivity_AD	The surface emissivity adjoint at vertical and horizontal polarizations	N/A	IN OUT
Temperature_AD	Sea surface temperature adjoint	(Kelvin) ⁻¹	IN OUT
Salinity_AD	Salinity of sea water adjoint	(% _o) ⁻¹	IN OUT
Wind_Speed_AD	Sea surface wind speed adjoint	(m.s ⁻¹) ⁻¹	IN OUT
iVar	Structure containing internal variables. Output from the forward model.	N/A	IN

Figure 2.3: Adjoint model interface and argument description for the low frequency microwave sea surface emissivity model.

3 Component Tests

3.1 Guillou Ocean Permittivity

The Guillou ocean permittivity model is taken from [Guillou et al. \[1998\]](#) where temperature and salinity dependent polynomimal fits for the conductivity, σ , the static permittivity, ϵ_s , the high frequency permittivity, ϵ_∞ , and the Debye relaxation time, τ , are used to produce complex permittivity values according to the Debye model. The emissivity model invokes the Guillou permittivity procedures only for frequencies less than 20GHz.

This section details the forward/tangent-linear and tangent-linear/adjoint tests performed on the Guillou ocean permittivity procedures. The number and range of input quantities used in the tests are shown in table 3.1. A selection of computed forward model Guillou permittivities at different frequencies are shown in figure 3.1.

Quantity	# of Values	Range	Units
Frequency	21	5.0 - 20.0	GHz
Salinity	21	20.0 - 40.0	%
Temperature	21	273.0 - 303.0	K

Table 3.1: Range of test input data to the Guillou ocean permittivity procedures.

3.1.1 FWD/TL Test Results

The description of the FWD/TL tests for routines with complex valued output was given in section 1.2.1. Some representative results for the Guillou permittivity routines are shown in figure 3.2 for 7.25GHz and an alpha value of 0.1, and in figure 3.3 for 16.25GHz and an alpha value of 0.0001. The maximum tolerance residual for each value of alpha is shown in table 3.2. As would be expected, as alpha decreases so do the tolerance

α	Tolerance residual, t_r
0.1	6.0e-08
0.01	6.0e-10
0.001	5.0e-11
0.0001	4.0e-10

Table 3.2: Maximum tolerance residuals for the Guillou permittivity FWD/TL tests.

residuals since, for smaller and smaller perturbations the forward model reponse becomes more linear, i.e. the residuals are more due to noise than non-linearity. This is quite evident when one compares the residual surfaces of figure 3.2(e) and (f) with those in figure 3.3(e) and (f). As the alpha value decreases, the residuals contain less information about the polynomial dependencies of the Guillou permittivity on temperature (higher orders) and salinity (linear). It is surmised that the $O(10^{-10})$ tolerance limit for the FWD/TL tests is due to the propagation of precision errors in the model parameterisation. In any case, the results are well below the precision of the measurements used in generating the fit coefficients as reported in [Guillou et al. \[1998\]](#).

3.1.2 TL/AD Test Results

Following the description of the TL/AD tests in section 1.2.2 for routines with real valued input and complex valued output, the TL/AD test performed for the Guillou permittivity routines was,

$$\underbrace{[\Re\{\delta\epsilon\}^2 + \Im\{\delta\epsilon\}^2]}_{\mathbf{TL}^T \mathbf{TL}} - \underbrace{[\delta T \cdot \delta^* T + \delta S \cdot \delta^* S]}_{\delta \mathbf{x}^T \mathbf{AD}(TL)} = 0 \quad (3.1)$$

where T and S are the sea surface temperature and salinity respectively (TL inputs are set to 0.1 in both cases), and ϵ is the complex permittivity. Examples of the intermediate and final quantities used in this test are shown

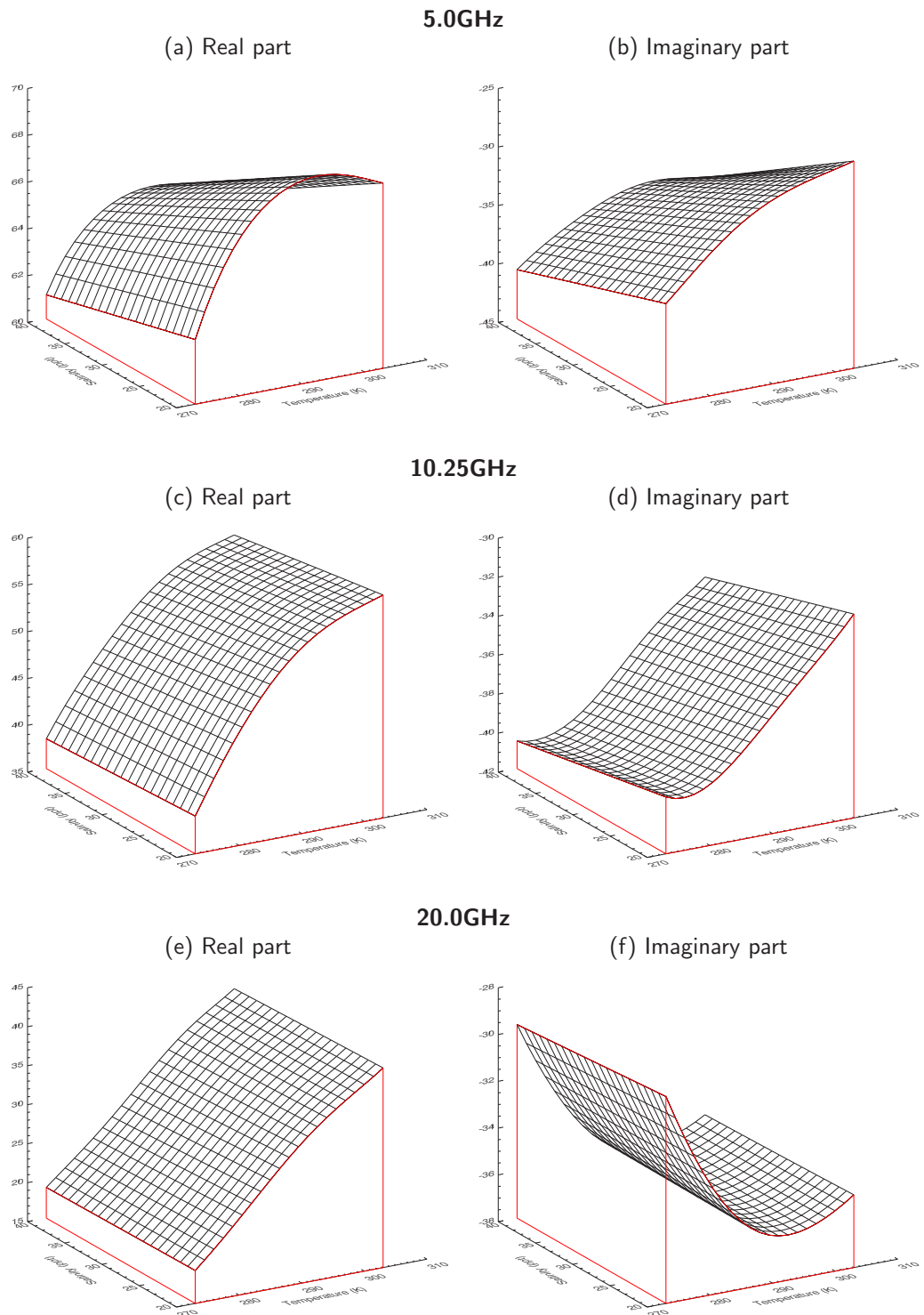
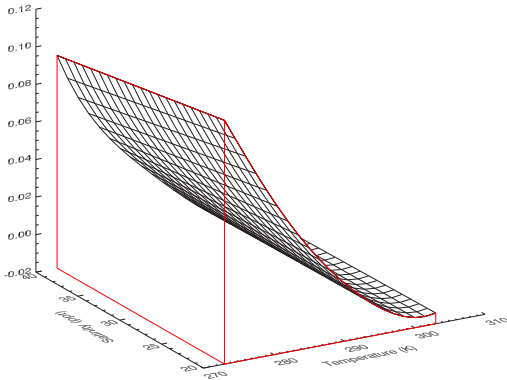


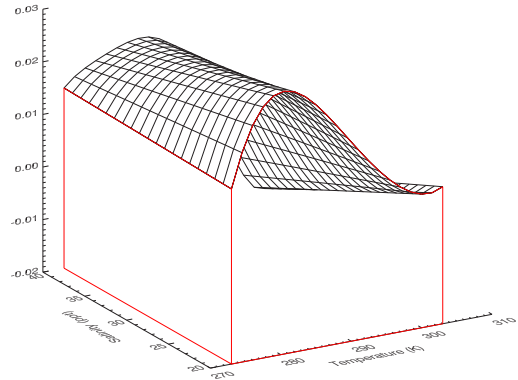
Figure 3.1: Real and imaginary parts of the computed Guillou permittivity as a function of temperature and salinity for three frequencies $\leq 20\text{GHz}$

Non-linear difference

(a) $\Delta \Re\{\epsilon\}$

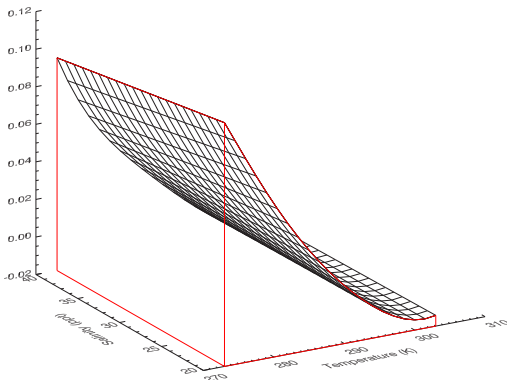


(b) $\Delta \Im\{\epsilon\}$

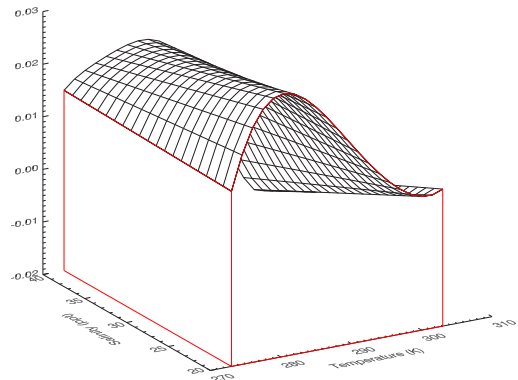


Tangent-linear response

(c) $\Re\{\delta\epsilon\}$

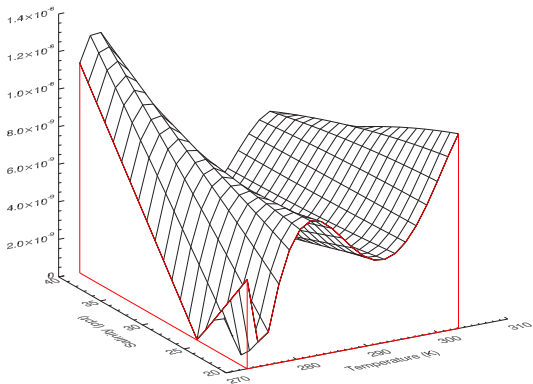


(d) $\Im\{\delta\epsilon\}$



Forward/tangent-linear test result

(e) $|\Delta \Re\{\epsilon\} - \Re\{\delta\epsilon\}|$



(f) $|\Delta \Im\{\epsilon\} - \Im\{\delta\epsilon\}|$

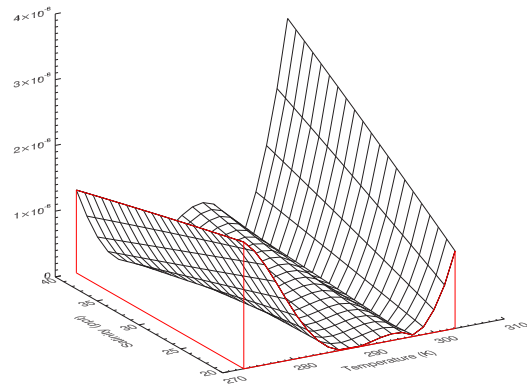
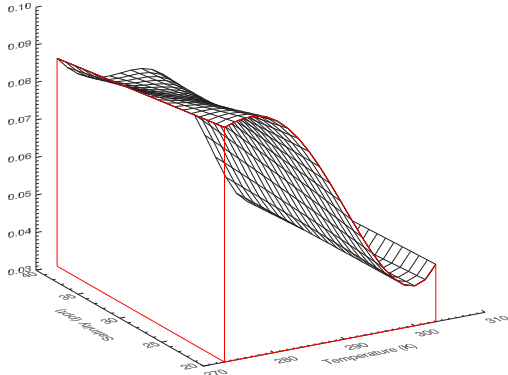


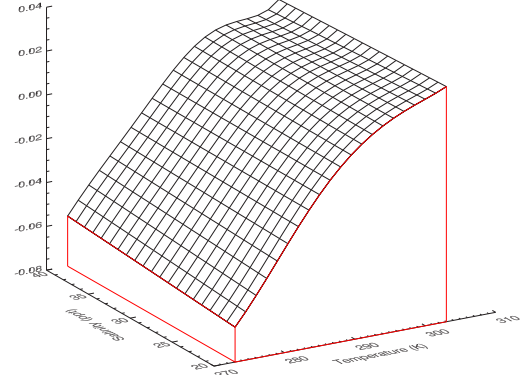
Figure 3.2: Real and imaginary parts of the computed Guillou complex permittivities at 7.25GHz for the forward/tangent-linear test with $\alpha=0.1$. (a) Real component non-linear difference. (b) Imaginary component non-linear difference. (c) Real component tangent-linear response. (d) Imaginary component tangent-linear response. (e) Real component test residual. (f) Imaginary component test residual.

Non-linear difference

(a) $\Delta \Re\{\epsilon\}$

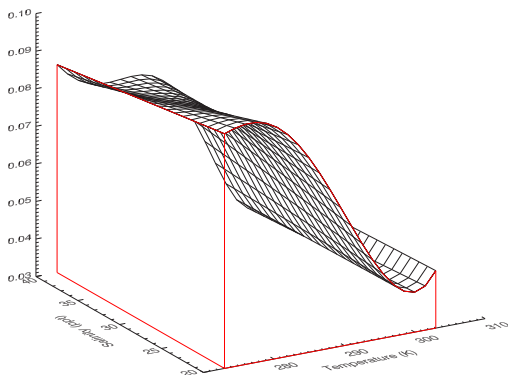


(b) $\Delta \Im\{\epsilon\}$

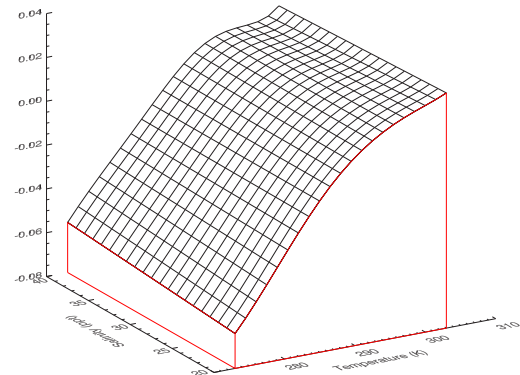


Tangent-linear response

(c) $\Re\{\delta\epsilon\}$

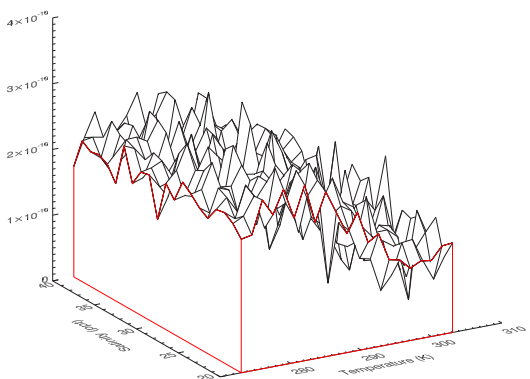


(d) $\Im\{\delta\epsilon\}$



Forward/tangent-linear test result

(e) $|\Delta \Re\{\epsilon\} - \Re\{\delta\epsilon\}|$



(f) $|\Delta \Im\{\epsilon\} - \Im\{\delta\epsilon\}|$

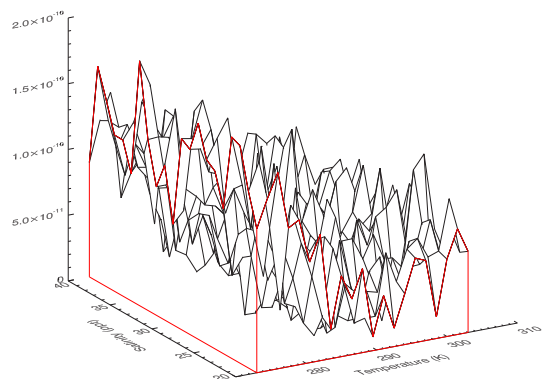


Figure 3.3: Real and imaginary parts of the computed Guillou complex permittivities at 16.25GHz for the forward/tangent-linear test with $\alpha=0.0001$. (a) Real component non-linear difference. (b) Imaginary component non-linear difference. (c) Real component tangent-linear response. (d) Imaginary component tangent-linear response. (e) Real component test residual. (f) Imaginary component test residual.

in figure 3.4 for $f = 7.25\text{GHz}$ and 3.5 for $f = 16.25\text{GHz}$. The differences between the values represented in figures 3.4(e) and (f) and 3.5(e) and (f) are shown in figure 3.6. In both cases, the differences were within numerical precision. These results are typical of the other frequencies tested.

3.2 Fresnel Reflectivity

The derivations of the Fresnel reflectivity equations used in the model are given in appendix A. This section details the forward/tangent-linear and tangent-linear/adjoint tests performed on the Fresnel reflectivity procedures. The number and range of input quantities used in the tests are shown in table 3.3. A selection of computed forward model reflectivities at different incidence angles are shown in figure 3.7.

Quantity	# of Values	Range	Units
Angle, θ_i	7	0.0 - 60.0	degrees
$\Re\{\epsilon\}$	21	5.0 - 75.0	F.m^{-1} (?)
$\Im\{\epsilon\}$	21	-5.0 - -31.0	F.m^{-1} (?)

Table 3.3: Range of test input data to the Fresnel reflectivity procedures.

3.2.1 FWD/TL Test Results

The description of the FWD/TL tests for routines with real valued output was given in section 1.2.1. Some representative results for the Fresnel reflectivity FWD/TL tests are shown in figure 3.8 for an incidence angle of 20° and an alpha value of 0.1 and in figure 3.9 for an incidence angle of 40° and an alpha value of 0.0001. The maximum tolerance residual for each value of alpha is shown in table 3.4. As with the permittivity FWD/TL

α	Tolerance residual, t_r
0.1	7.0e-09
0.01	7.0e-11
0.001	7.0e-13
0.0001	3.0e-12

Table 3.4: Maximum tolerance residuals for the Fresnel reflectivity FWD/TL tests.

test, as the alpha value decreases so does the tolerance residual. Interestingly, the tolerance residual for the smallest alpha value follows the same pattern as for the permittivity in that it is an order of magnitude larger than that for the next larger alpha value case. Additional tests showed that as alpha is decreased even further, the associated tolerance residual steadily increases indicating the results are at the precision limit.

3.2.2 TL/AD Test Results

Following the description of the TL/AD test in section 1.2.2 for routines with complex valued input and real valued output, the TL/AD test performed for the Fresnel reflectivity routines was,

$$\underbrace{[\delta r_v^2 + \delta r_h^2]}_{\mathbf{TL}^T \mathbf{TL}} - \underbrace{[\Re\{\delta\epsilon\} \Re\{\delta^*\epsilon\} + \Im\{\delta\epsilon\} \Im\{\delta^*\epsilon\}]}_{\delta \mathbf{x}^T \mathbf{AD}(TL)} = 0 \quad (3.2)$$

where ϵ is the complex permittivity (TL inputs set to 0.1), and r_v and r_h are the vertical and horizontal reflectivities respectively. Examples of the intermediate and final quantities used in this test are shown in figure 3.10 for $\theta_i = 20^\circ$, and figure 3.11 for $\theta_i = 40^\circ$. The differences between figure 3.10(e) and (f), and figure 3.11(e) and (f) are shown in figure 3.12. In both cases, the differences are within numerical precision. These results are typical of the other incidence angles tested.

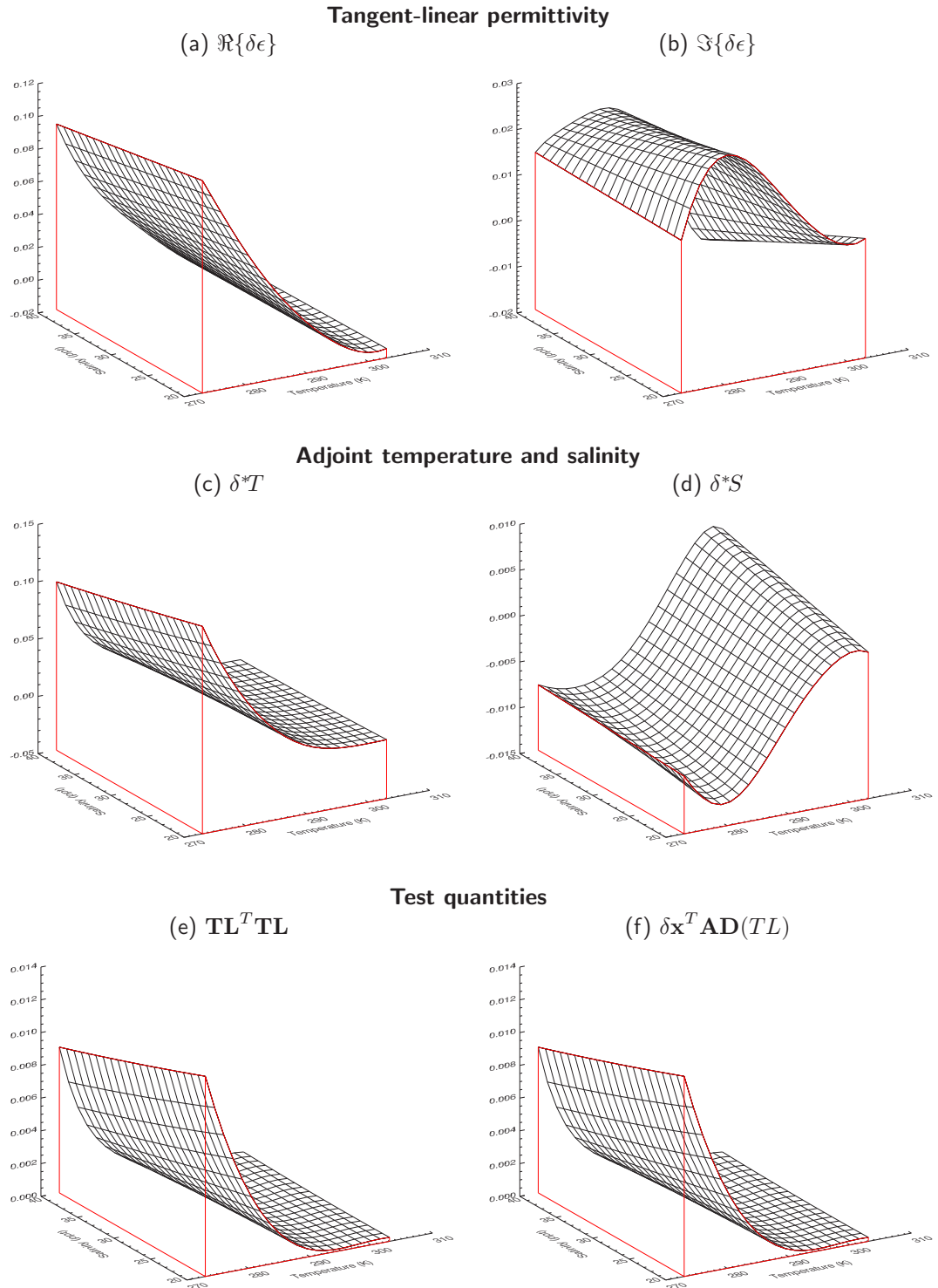


Figure 3.4: Example of quantities used to test the TL/AD Guillou permittivity routines for δT and δS inputs of 0.1 at 7.25GHz. (a) Real component of the tangent-linear permittivity. (b) Imaginary component of the tangent-linear permittivity. (c) Temperature adjoint. (d) Salinity adjoint. (e) Tangent-linear test result (see eqn.3.1). (f) Adjoint test result (see eqn.3.1).

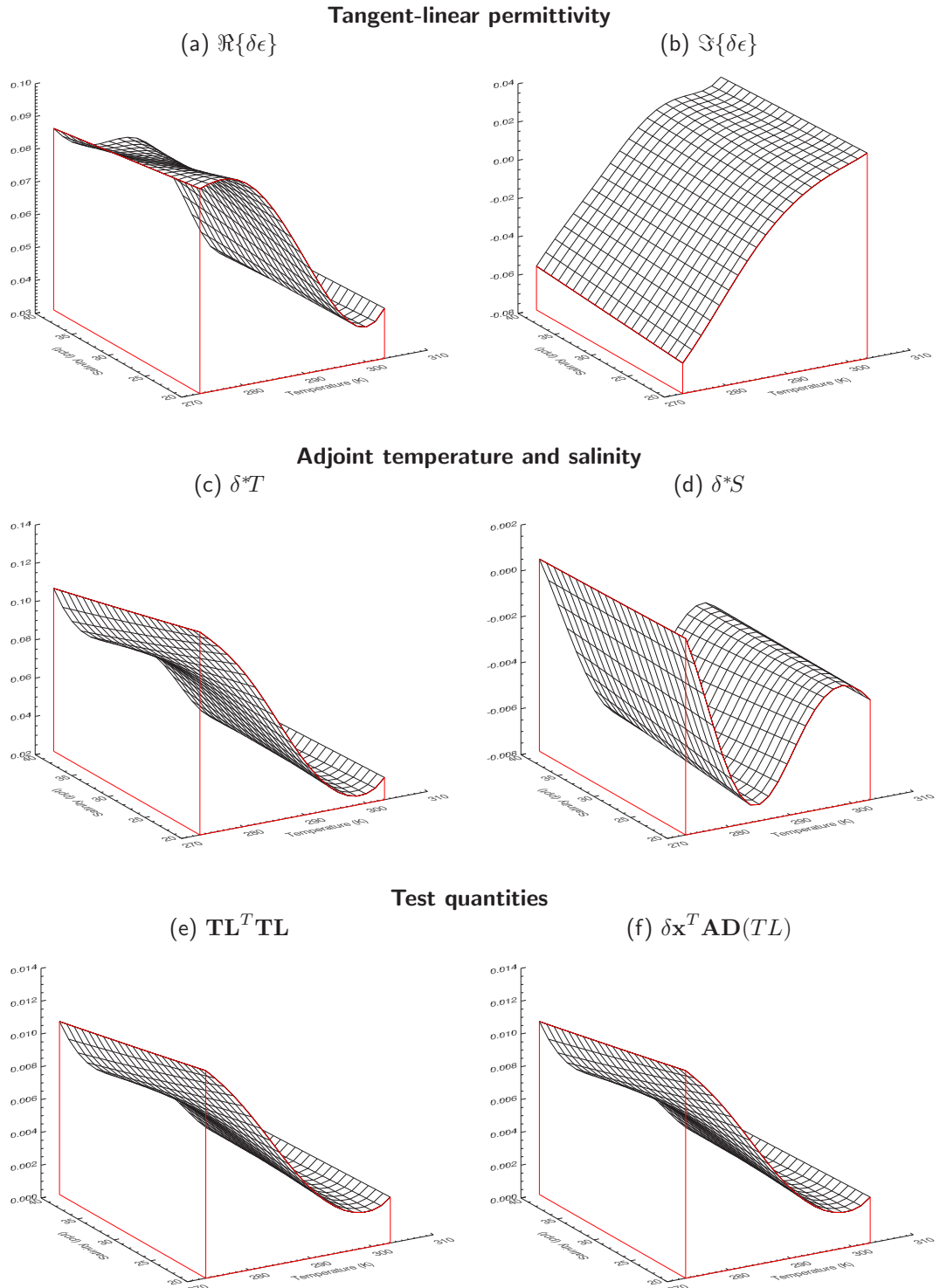


Figure 3.5: Example of quantities used to test the TL/AD Guillou permittivity routines for δT and δS inputs of 0.1 at 16.25GHz. **(a)** Real component of the tangent-linear permittivity. **(b)** Imaginary component of the tangent-linear permittivity. **(c)** Temperature adjoint. **(d)** Salinity adjoint. **(e)** Tangent-linear test result (see eqn.3.1). **(f)** Adjoint test result (see eqn.3.1).

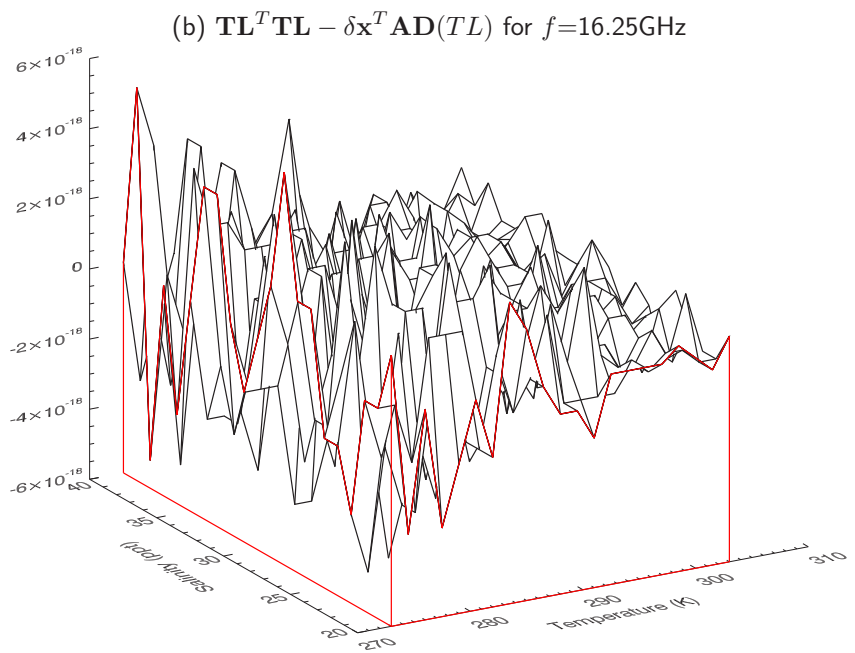
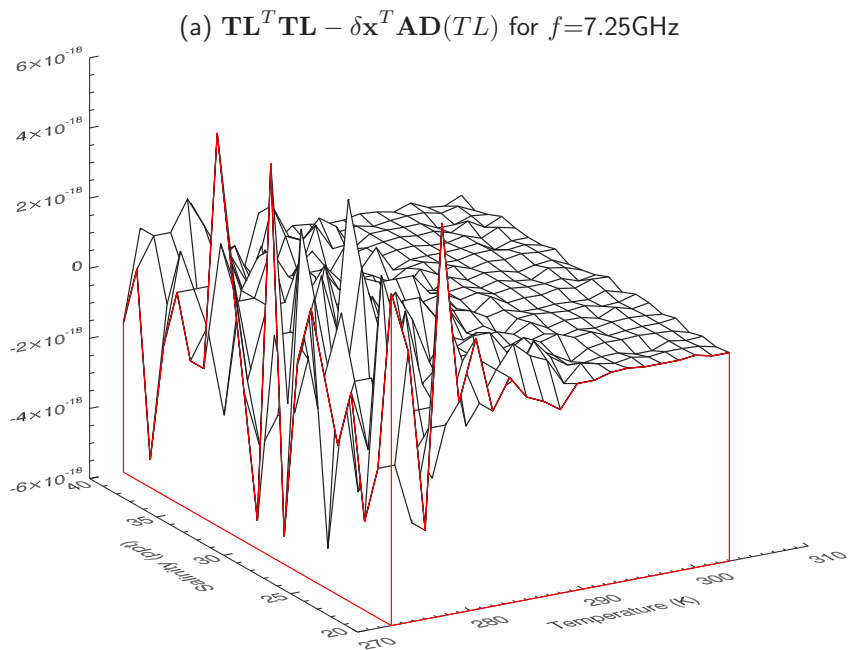


Figure 3.6: Guillou permittivity model TL/AD test results for the two test frequencies indicating TL/AD agreement to numerical precision. **(a)** Result for 7.25GHz (See figure 3.4). **(b)** Result for 16.25GHz (See figure 3.5).

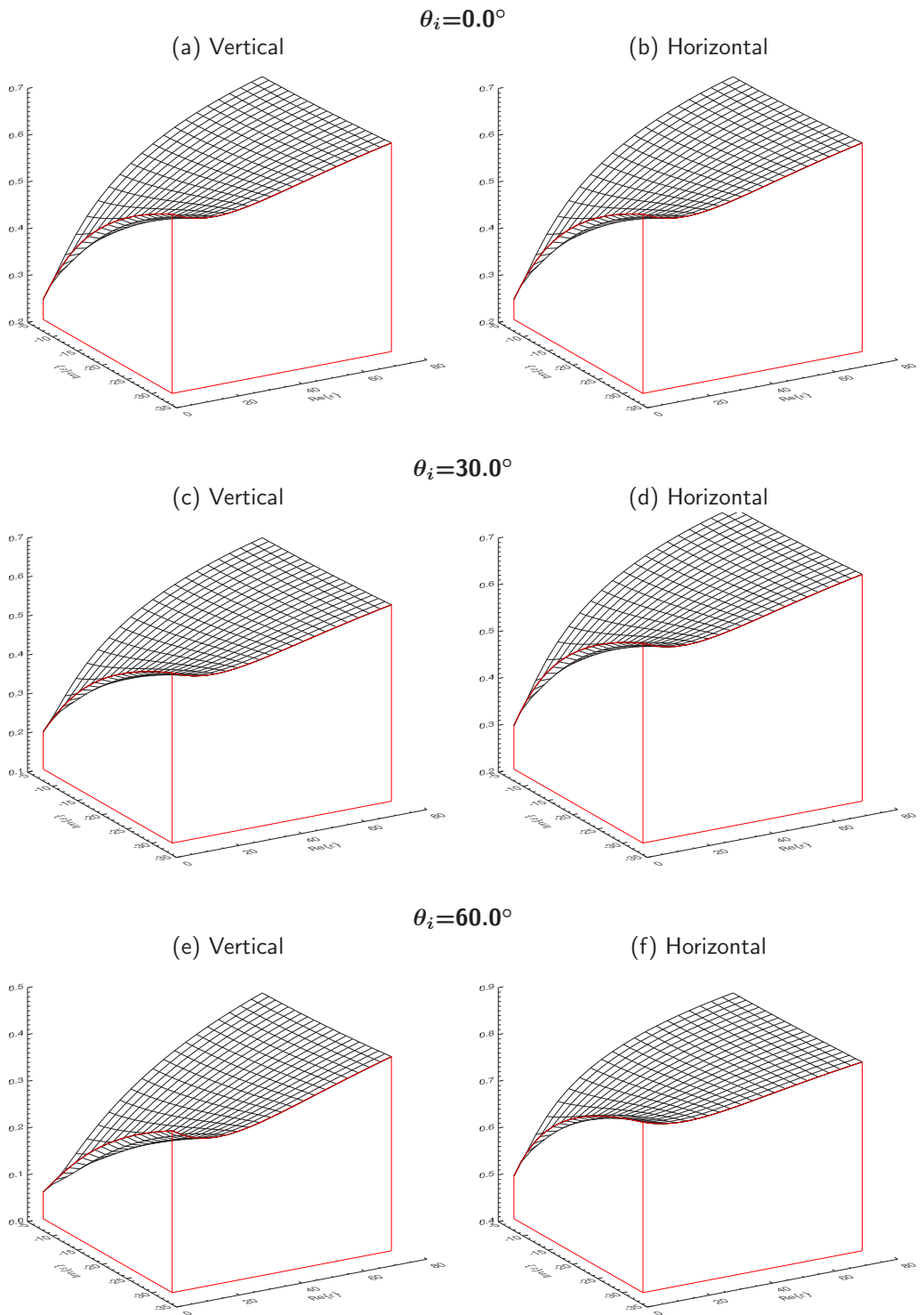


Figure 3.7: Vertical and horizontal Fresnel reflectivities as a function of the real and imaginary part of the permittivity for three incidence angles.

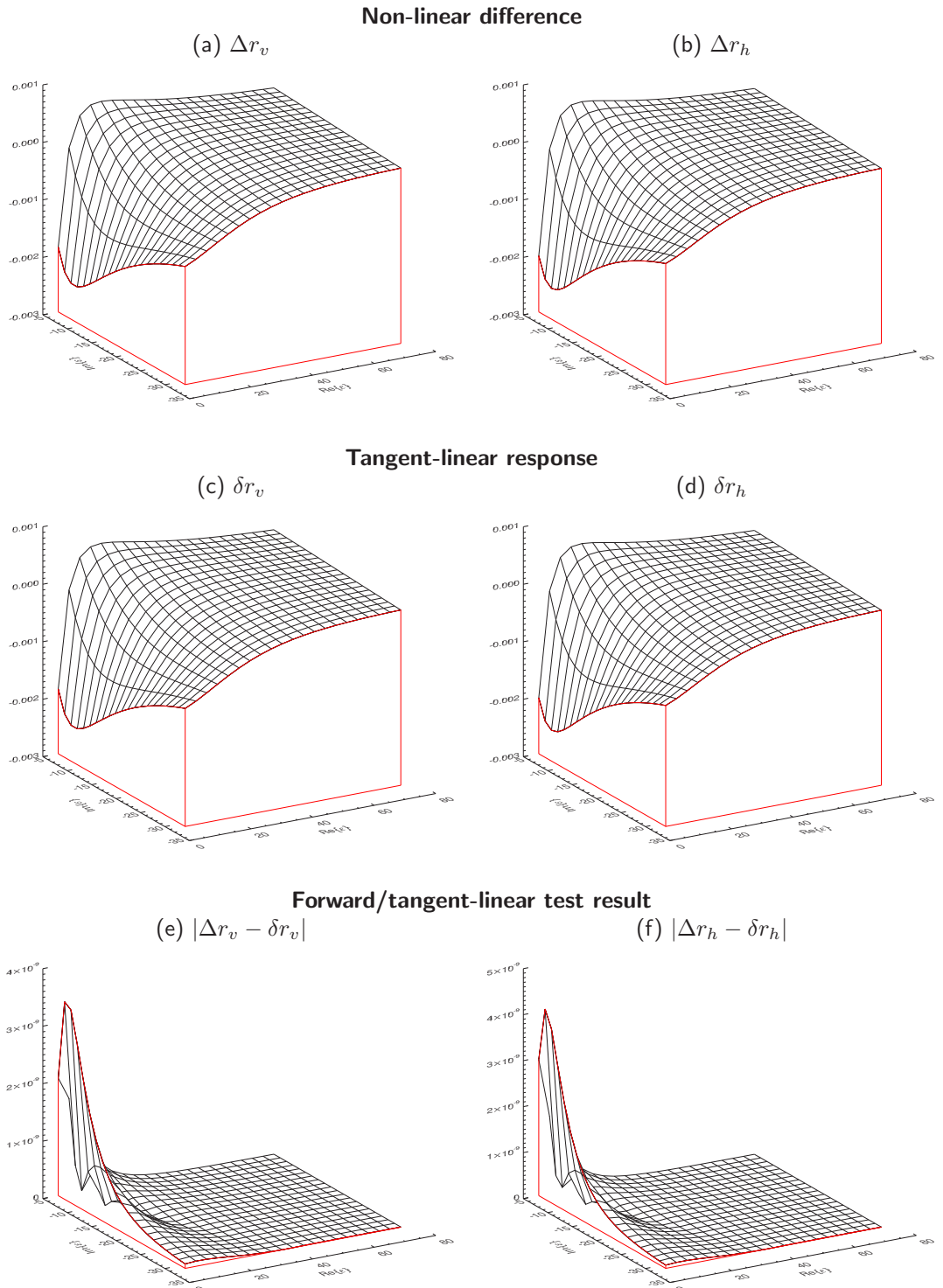
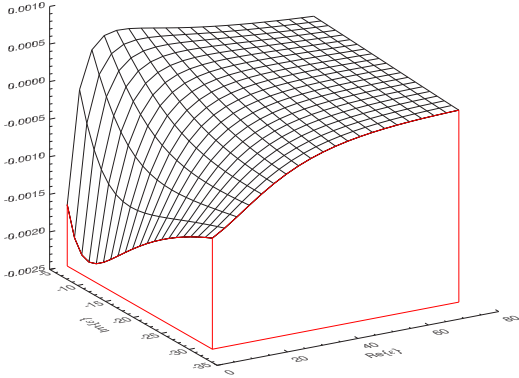


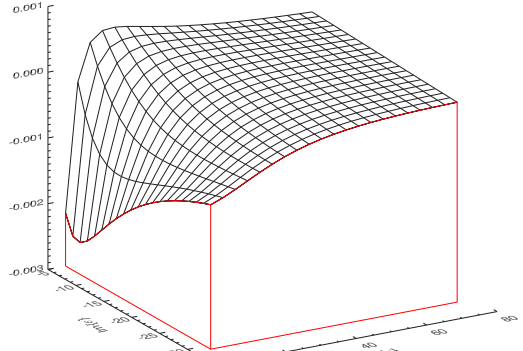
Figure 3.8: Vertical and horizontal Fresnel reflectivities at $\theta_i=20.0^\circ$ for the forward/tangent-linear test with $\alpha=0.1$. (a) Vertical component non-linear difference. (b) Horizontal component non-linear difference. (c) Vertical component tangent-linear response. (d) Horizontal component tangent-linear response. (e) Vertical component test residual. (f) Horizontal component test residual.

Non-linear difference

(a) Δr_v

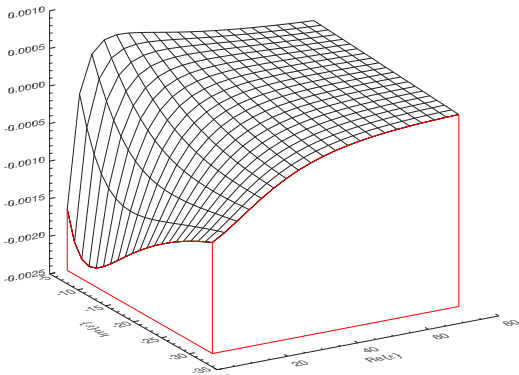


(b) Δr_h

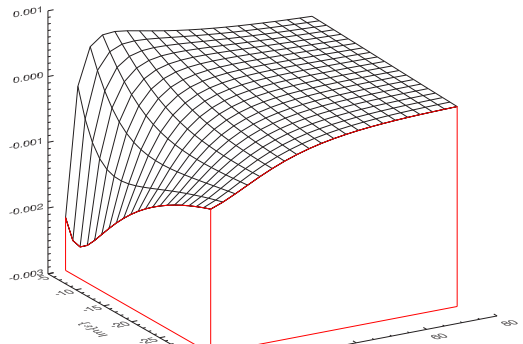


Tangent-linear response

(c) δr_v

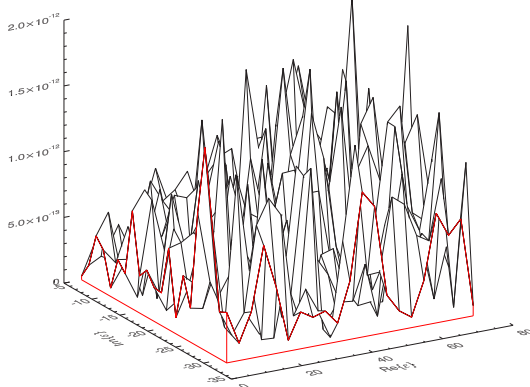


(d) δr_h



Forward/tangent-linear test result

(e) $|\Delta r_v - \delta r_v|$



(f) $|\Delta r_h - \delta r_h|$

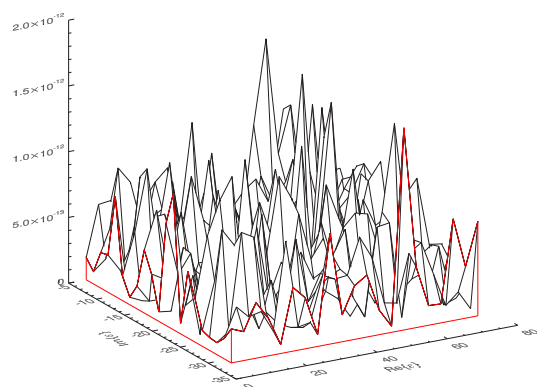
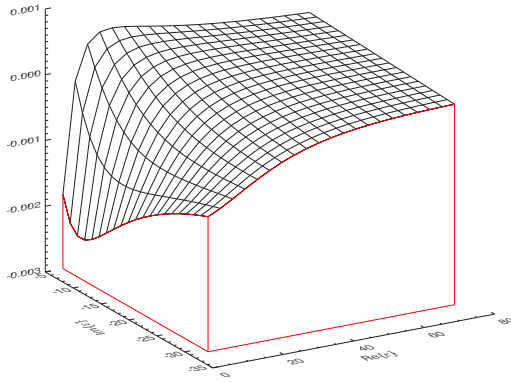


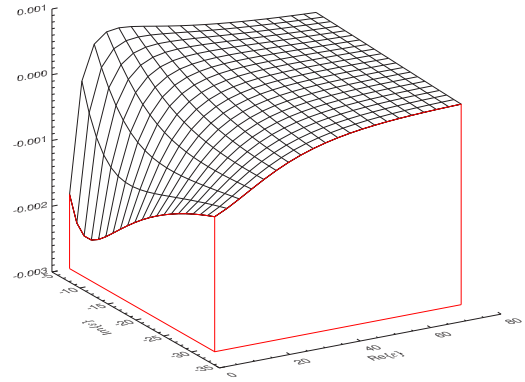
Figure 3.9: Vertical and horizontal Fresnel reflectivities at $\theta_i=40.0^\circ$ for the forward/tangent-linear test with $\alpha=0.0001$. (a) Vertical component non-linear difference. (b) Horizontal component non-linear difference. (c) Vertical component tangent-linear response. (d) Horizontal component tangent-linear response. (e) Vertical component test residual. (f) Horizontal component test residual.

Tangent-linear reflectivities

(a) δr_v

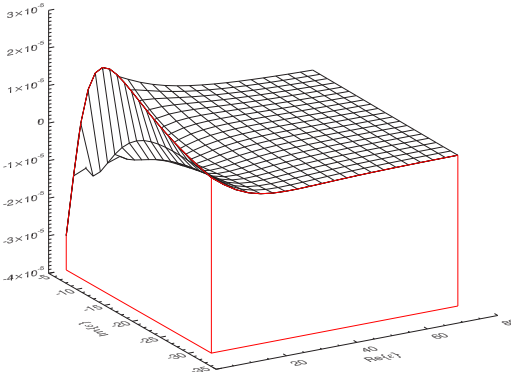


(b) δr_h

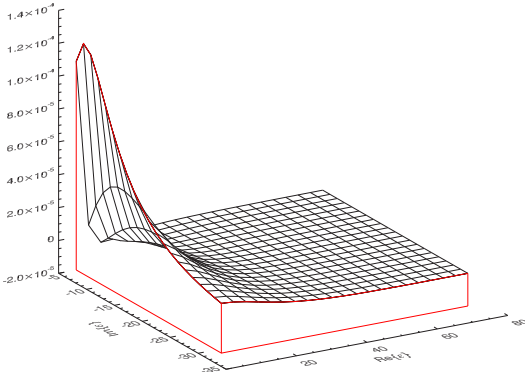


Adjoint permittivities

(c) $\Re\{\delta^*\epsilon\}$

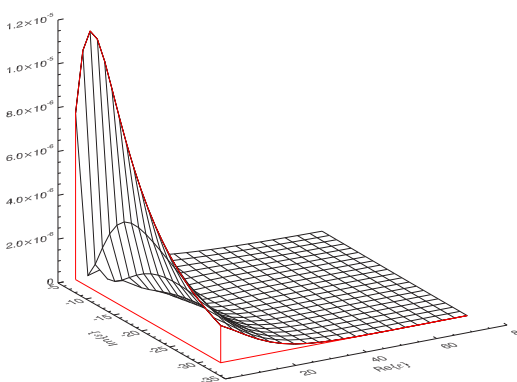


(d) $\Im\{\delta^*\epsilon\}$



Test quantities

(e) $\mathbf{TL}^T \mathbf{TL}$



(f) $\delta \mathbf{x}^T \mathbf{AD}(TL)$

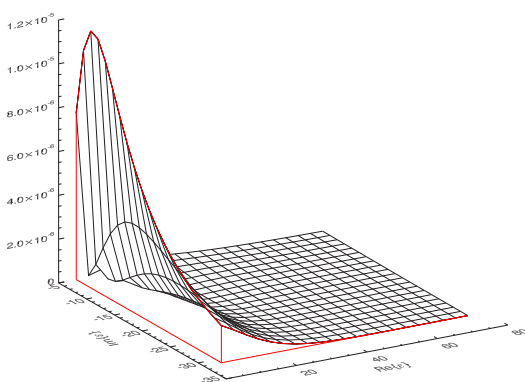
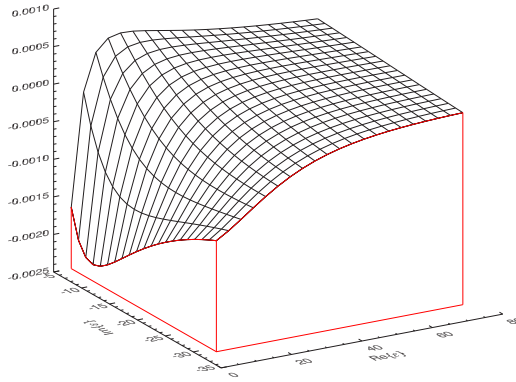


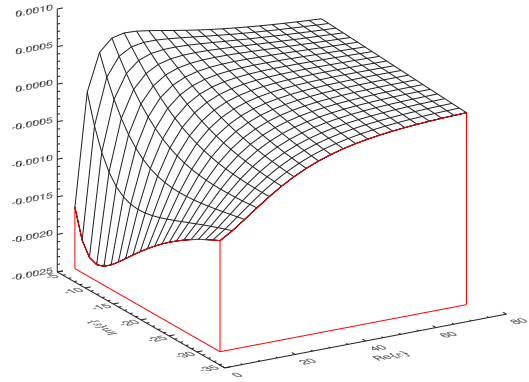
Figure 3.10: Example of quantities used to test the TL/AD Fresnel reflectivity routines for $\Re\{\delta\epsilon\}$ and $\Im\{\delta\epsilon\}$ inputs of 0.1 at an incidence angle of 20° . **(a)** Tangent-linear vertical reflectivity. **(b)** Tangent-linear horizontal reflectivity. **(c)** Real component of the adjoint permittivity. **(d)** Imaginary component of the adjoint permittivity. **(e)** Tangent-linear test result (see eqn.3.2). **(f)** Adjoint test result (see eqn.3.2).

Tangent-linear reflectivities

(a) δr_v

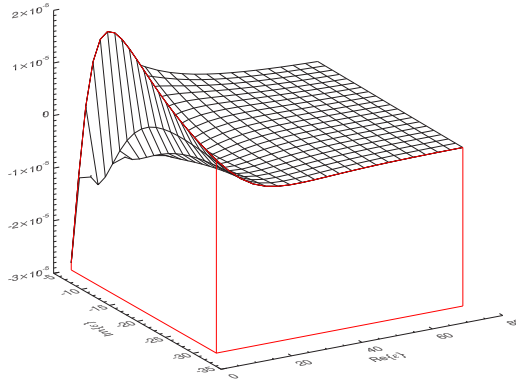


(b) δr_h

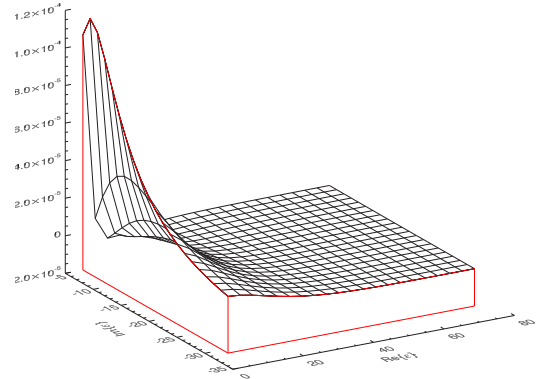


Adjoint permittivities

(c) $\Re\{\delta^*\epsilon\}$

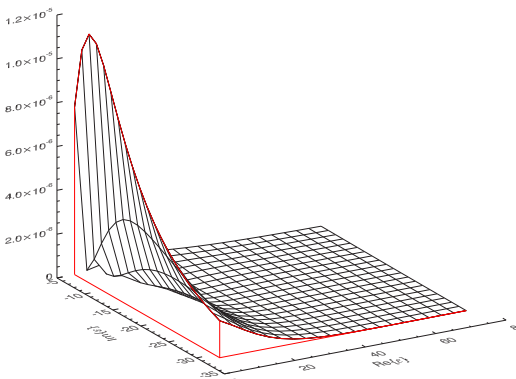


(d) $\Im\{\delta^*\epsilon\}$



Test quantities

(e) $\mathbf{TL}^T \mathbf{TL}$



(f) $\delta \mathbf{x}^T \mathbf{AD}(TL)$

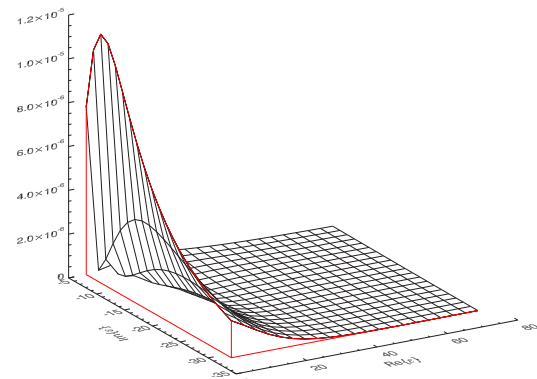


Figure 3.11: Example of quantities used to test the TL/AD Fresnel reflectivity routines for $\Re\{\delta\epsilon\}$ and $\Im\{\delta\epsilon\}$ inputs of 0.1 at an incidence angle of 40°. **(a)** Tangent-linear vertical reflectivity. **(b)** Tangent-linear horizontal reflectivity. **(c)** Real component of the adjoint permittivity. **(d)** Imaginary component of the adjoint permittivity. **(e)** Tangent-linear test result (see eqn.3.2). **(f)** Adjoint test result (see eqn.3.2).

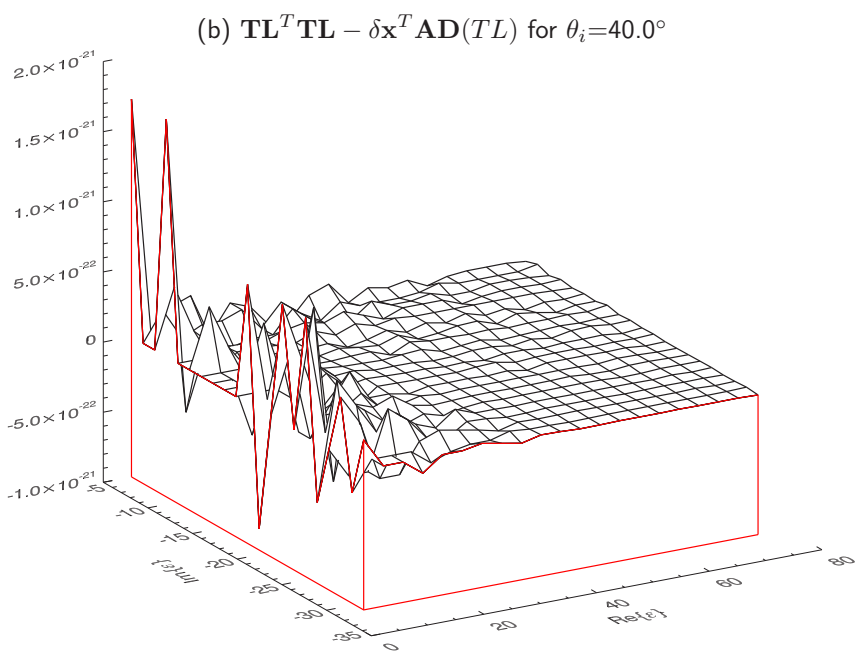
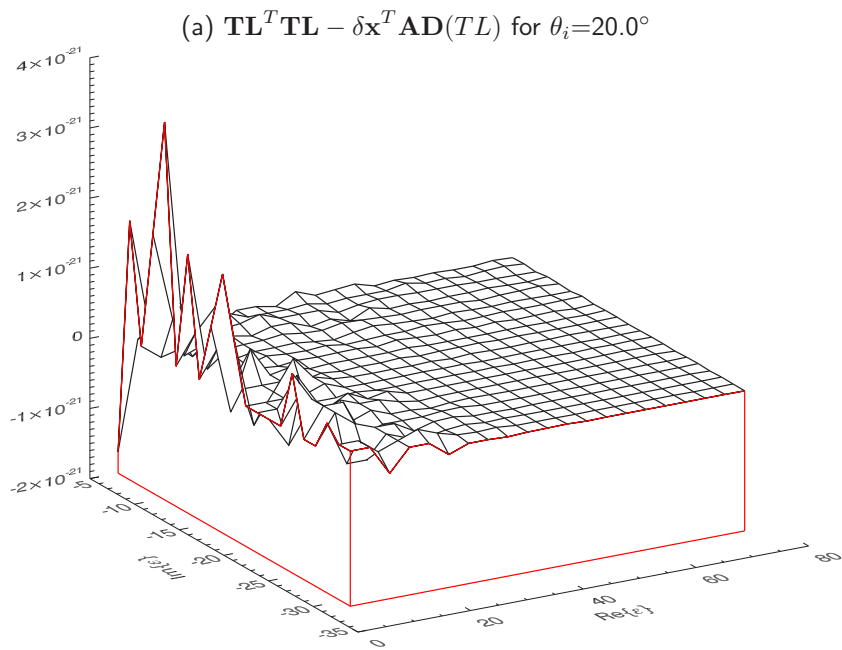


Figure 3.12: Fresnel reflectivity model TL/AD test results for the two test incidence angles indicating TL/AD agreement to numerical precision. **(a)** Result for 20° (See figure 3.10). **(b)** Result for 40° (See figure 3.11).

4 Model Test

This section details the forward/tangent-linear and tangent-linear/adjoint tests performed on the main subroutines: `LowFrequency_MWSSEM()`, `LowFrequency_MWSSEM_TL()`, and `LowFrequency_MWSSEM_AD()`. The number of input test values and their ranges of the input forward variables are shown in table 4.1. The actual values used are evenly distributed between the minimum and maximum, inclusively. The number of frequency and wind

Quantity	# of Values	Range	Units
Frequency	16	5.0 - 20.0	GHz
Zenith angle	7	0.0 - 60.0	Deg.
Temperature	11	273.0 - 303.0	K
Salinity	5	20.0 - 40.0	%
Wind speed	21	2.0 - 19.0	m.s^{-1}

Table 4.1: Range of test input data to main LF MWSSEM routines

speed values were chosen such that there was not always correspondence with the hinge points of the ocean height variance lookup table (LUT). This ensures that the interpolation of the LUT data is included in the testing.

Forward model results for two test frequencies (7.0GHz and 19.0GHz)², one zenith angle (30°), and one salinity value (35%) are shown in figure 4.1. As mentioned in section 1.1, for wind speeds greater than 7.0ms^{-1} the Fresnel reflectivities are modified to account for surface foam and this shows up in the forward results as a discontinuity between 7.0 and 8.0ms^{-1} (most evident in figure 4.1(b)).

4.1 FWD/TL Test Results

The description of the FWD/TL tests for routines with real valued output is given in section 1.2.1. Some representative results are shown in figure 4.2 for 7.0GHz and an alpha value of 0.1. The aforementioned discontinuity seen at wind speeds of 7.0ms^{-1} is quite evident in the non-linear and tangent-linear responses (figures 4.2(a)-(d)). The relatively large value of alpha means the perturbation is also relatively large and as such, the test residuals of figures 4.2(e) and (f) still exhibit some functional characteristics. When the value of alpha is decreased to 0.0001, while the responses themselves appear similar, the test residuals decrease to the point where it appears calculation “noise” predominates, as shown in figure 4.3. This is expected as the perturbation applied is much smaller and thus the forward model response is correspondingly more linear. The maximum tolerance residual for each value of alpha is shown in table 4.2. As expected, as alpha decreases so do the tolerance residuals since.

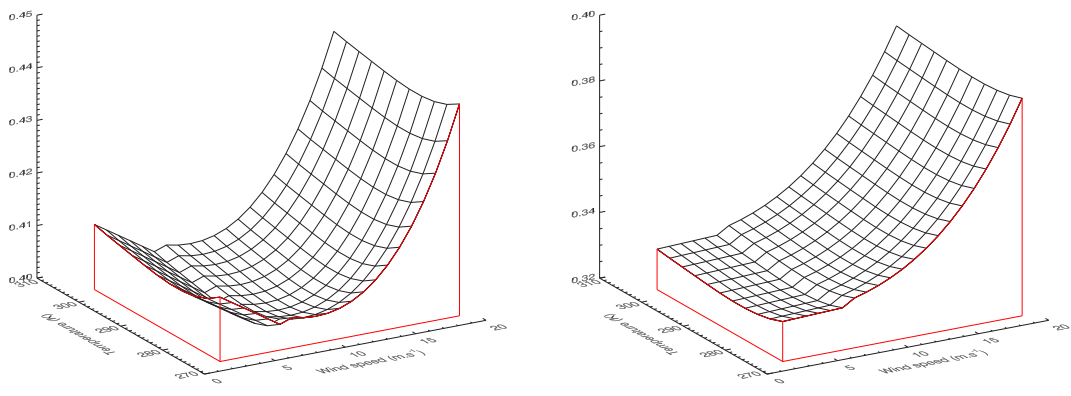
α	Tolerance residual, t_r
0.1	2.0e-06
0.01	2.0e-07
0.001	2.0e-08
0.0001	2.0e-09

Table 4.2: Maximum tolerance residuals for the emissivity FWD/TL tests.

Test results for an alpha value of 0.1 but for a frequency of 19.0GHz are shown in figure 4.4. The character of the non-linear and tangent-linear responses is very different to that seen for the 7.0GHz case. The unevenness seen along the wind speed dimension is due to the small scale correction applied for frequencies greater than 15GHz. Smaller residuals, but with the same characteristics spikes, were seen for the 19.0GHz case but with an alpha value of 0.0001, as shown in figure 4.5.

²AMSR-E channel 1 and 3 frequencies are 6.925GHz and 18.7GHz respectively.

$f=7.0\text{GHz}$, $\theta_i=30^\circ$, $S=35\%$



$f=19.0\text{GHz}$, $\theta_i=30^\circ$, $S=35\%$

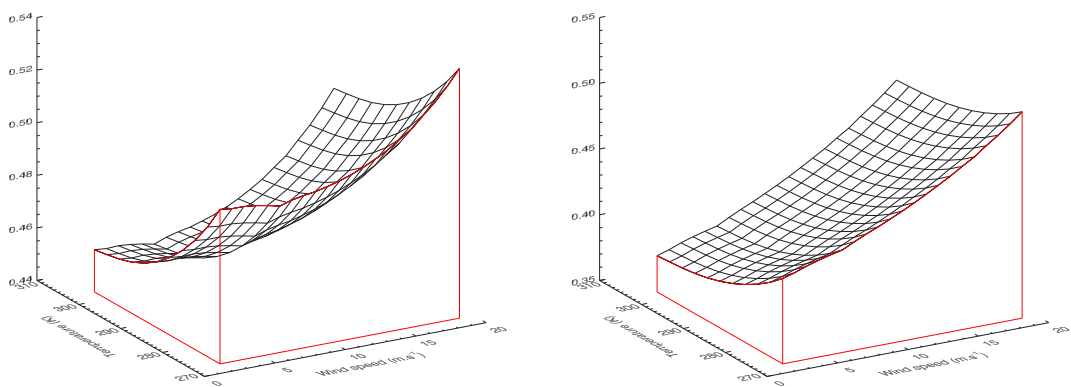


Figure 4.1: Computed vertical and horizontal polarised emissivities at two frequencies $< 20\text{GHz}$, a zenith angle of 30° , a salinity of 35% , and for a range of ocean surface wind speeds and temperatures. The feature seen at 7m.s^{-1} is due to the modification of the reflectivity due to foam cover.

As described in section 1.1.1, the ocean height variance is used in the small-scale reflectivity correction. Figure 4.6(a) shows the ocean height variance as a function of wind speed for various frequencies. Although they appear relatively smooth, removal of the mean slope, as shown in figure 4.6(b), shows how noisy the data is, which translates to the perturbation surfaces of figure 4.4. Additionally, the large spikes in the test residuals of figures 4.4(e) and (f) occur at wind speeds of 2.0, 10.5, and 19.0ms^{-1} which are all hingepoints in the ocean height variance LUT.

To determine if the noisy height displacement data is the cause of these wind speed hingepoint spikes, the data was smoothed using a Savitsky-Golay filter (see chapter 14 of Press et al. [1992]) of width 6ms^{-1} and 40GHz in the wind speed and frequency dimensions respectively. The smoothed height variance mean difference wind speed spectra are shown in figure 4.7. The FWD/TL residuals using this smoothed data are shown in figure 4.8 where they are approximately 2-10 times less than those using the original data, but still exhibit the anomalous peaks at the wind speed hingepoints.

Repeating the tests for different wind speed grids such that interpolation was performed primarily between, and not across, hingepoints led to the residuals shown in figure 4.9. Only the vertically polarised results are shown. Two tests were run: one where the edge value wind speeds were selected to not coincide with a LUT hingepoint but an intermediate value of 10.5ms^{-1} did, as seen in figure 4.9(a); and one where there were no test wind speed values near LUT hingepoints, as seen in figure 4.9(b). It appears that the forward model is particularly sensitive to perturbations about the LUT wind speed hingepoints, even when using the smoothed data.

Because perturbations along the temperature dimension do not exhibit the same behaviour, it suggests the integrations done on the ocean wave spectra of Bjerkaas and Riedel [1979] to derive the various height variance values, ζ_R^2 , should be recomputed. Since the residuals are of the order of 0.05% it may be unnecessary, but it does make objective validation of the tangent-linear model difficult.

4.2 TL/AD Test Results

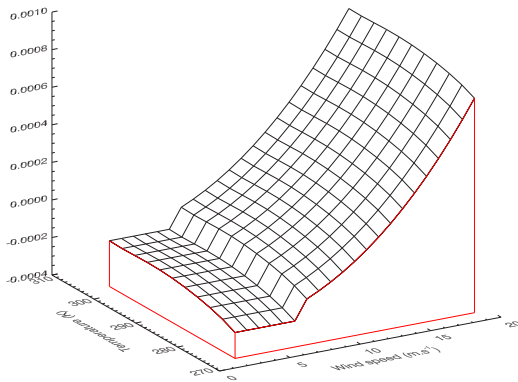
Following the description of the TL/AD test in section 1.2.2 for routines with both real valued input and output, the TL/AD test performed for the model was,

$$\underbrace{[\delta e_v^2 + \delta e_h^2]}_{\mathbf{TL}^T \mathbf{TL}} - \underbrace{[\delta T \cdot \delta^* T + \delta S \cdot \delta^* S + \delta W \cdot \delta^* W]}_{\delta \mathbf{x}^T \mathbf{AD}(TL)} = 0 \quad (4.1)$$

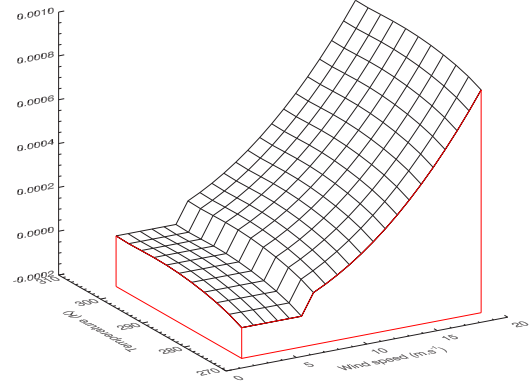
where T, S, and W are the sea surface temperature, salinity, and surface wind speed respectively (TL inputs are set to 0.1 in all cases); and e_v and e_h are the vertically and horizontally polarised sea surface emissivities. Examples of the intermediate quantities and test residual used in this test are shown in figure 4.10 for $f = 7.0\text{GHz}$ and figure 4.11 for $f = 19.0\text{GHz}$, both for salinities of 35%. In both cases, the residual differences are within numerical precision. Additionally, these results are typical for other frequencies and salinities tested.

Non-linear difference

(a) Δe_v

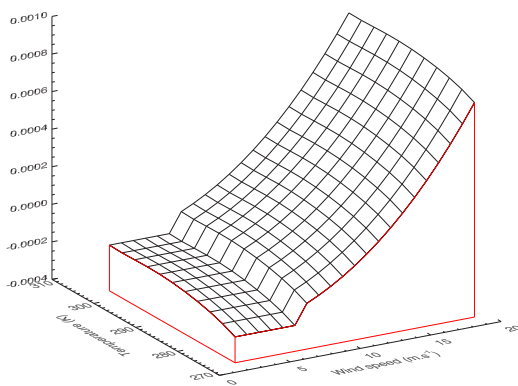


(b) Δe_h

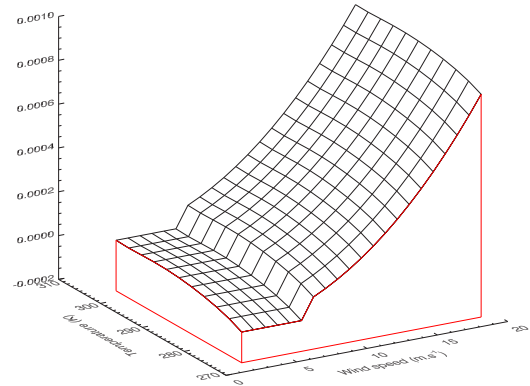


Tangent-linear response

(c) δe_v

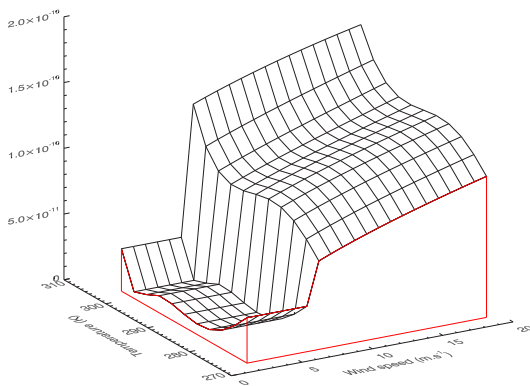


(d) δe_h



Forward/tangent-linear test result

(e) $|\Delta e_v - \delta e_v|$



(f) $|\Delta e_h - \delta e_h|$

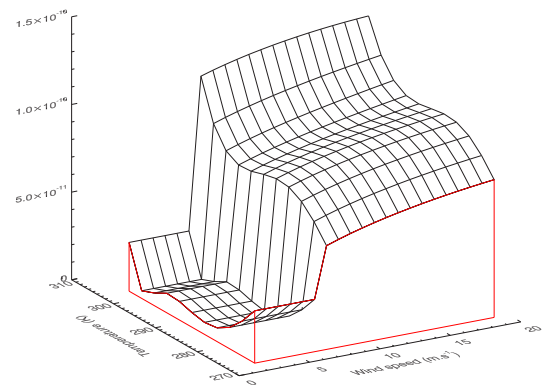


Figure 4.2: Computed emissivities at 7GHz for the forward/tangent-linear test with $\alpha=0.1$. **(a)** Vertically polarised non-linear difference. **(b)** Horizontally polarised non-linear difference. **(c)** Vertically polarised tangent-linear response. **(d)** Horizontally polarised tangent-linear response. **(e)** Vertically polarised test residual. **(f)** Horizontally polarised test residual.

Forward/tangent-linear test result

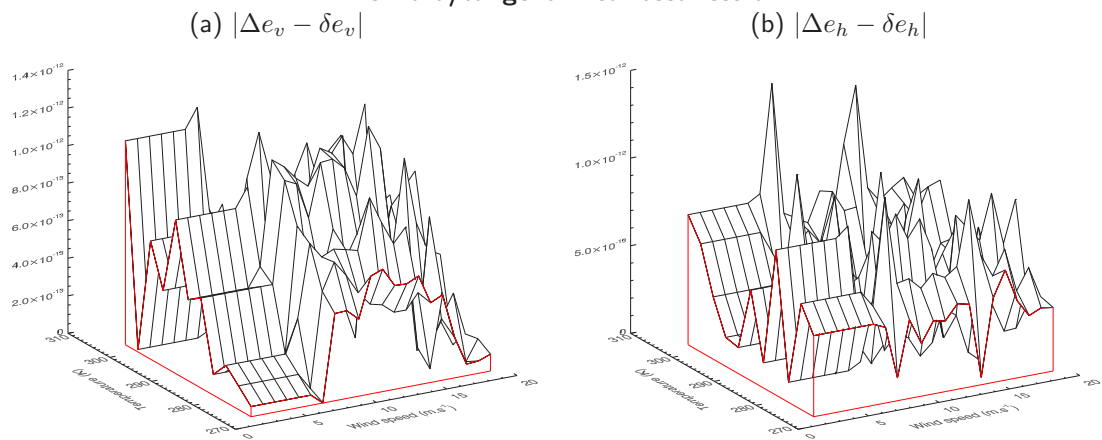


Figure 4.3: Forward/tangent-linear test residuals at 7GHz for $\alpha=0.0001$. **(a)** Vertically polarised test residual (compare with figure 4.2(e)). **(b)** Horizontally polarised test residual (compare with figure 4.2(f)).

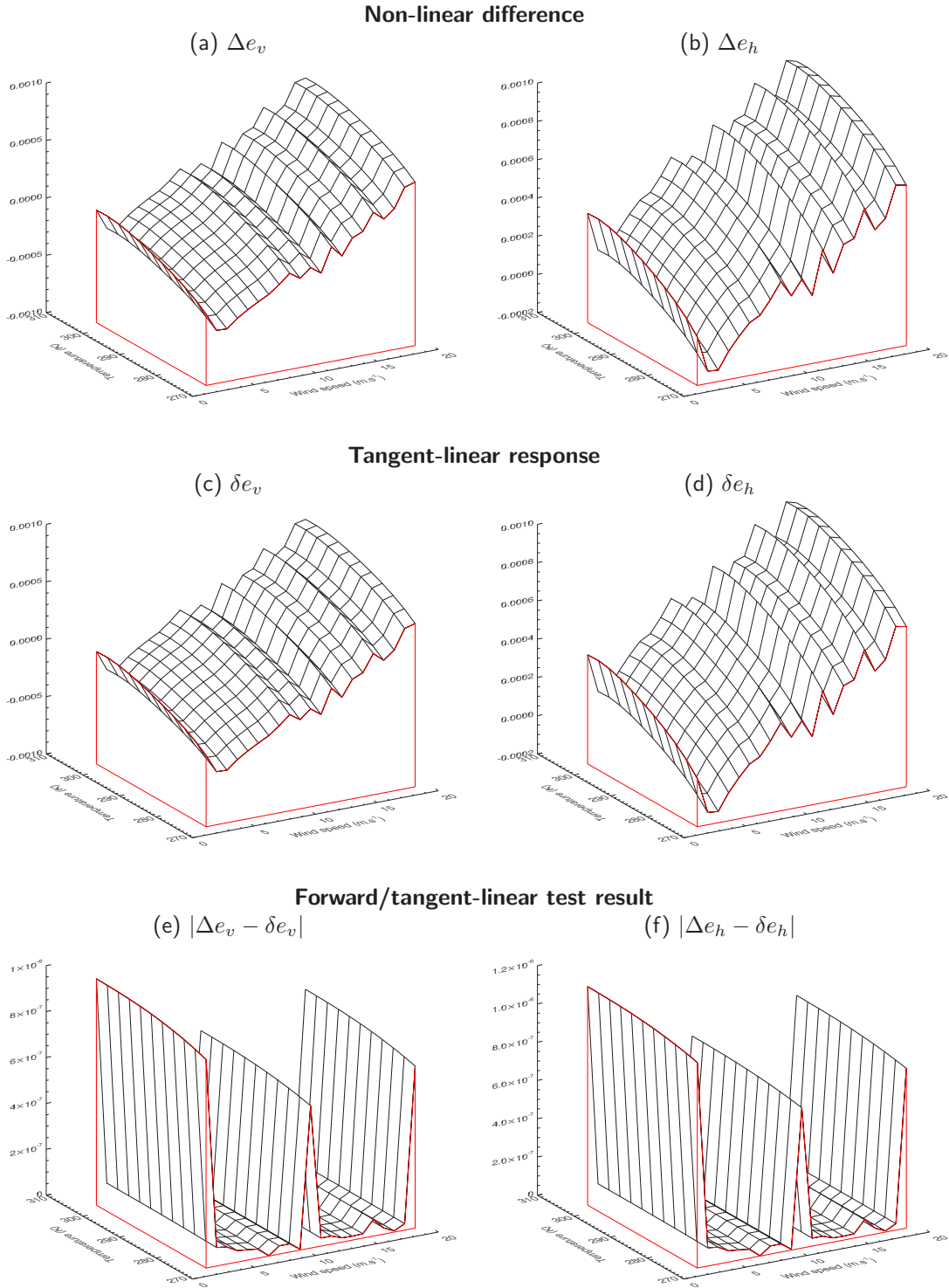


Figure 4.4: Computed emissivities at 19GHz for the forward/tangent-linear test with $\alpha=0.1$. **(a)** Vertically polarised non-linear difference. **(b)** Horizontally polarised non-linear difference. **(c)** Vertically polarised tangent-linear response. **(d)** Horizontally polarised tangent-linear response. **(e)** Vertically polarised test residual. **(f)** Horizontally polarised test residual.

Forward/tangent-linear test result

(a) $|\Delta e_v - \delta e_v|$ (b) $|\Delta e_h - \delta e_h|$

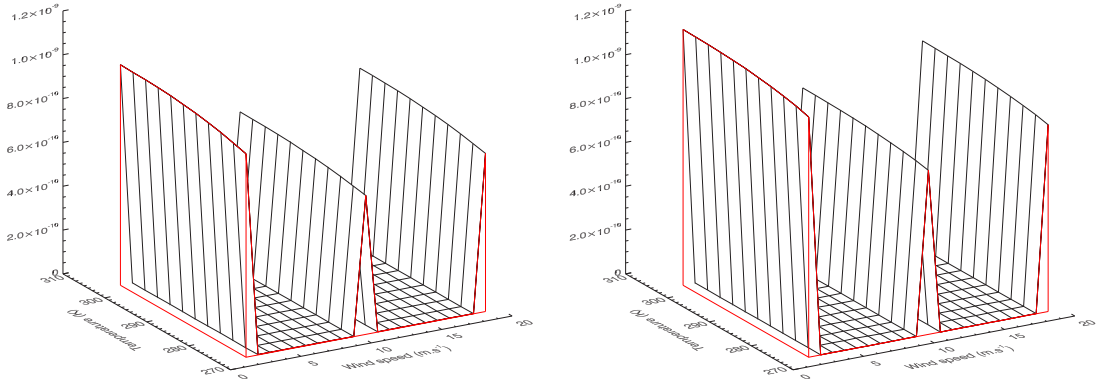


Figure 4.5: Forward/tangent-linear test residuals at 19GHz for $\alpha=0.0001$. **(a)** Vertically polarised test residual (compare with figure 4.4(e)). **(b)** Horizontally polarised test residual (compare with figure 4.4(f)).

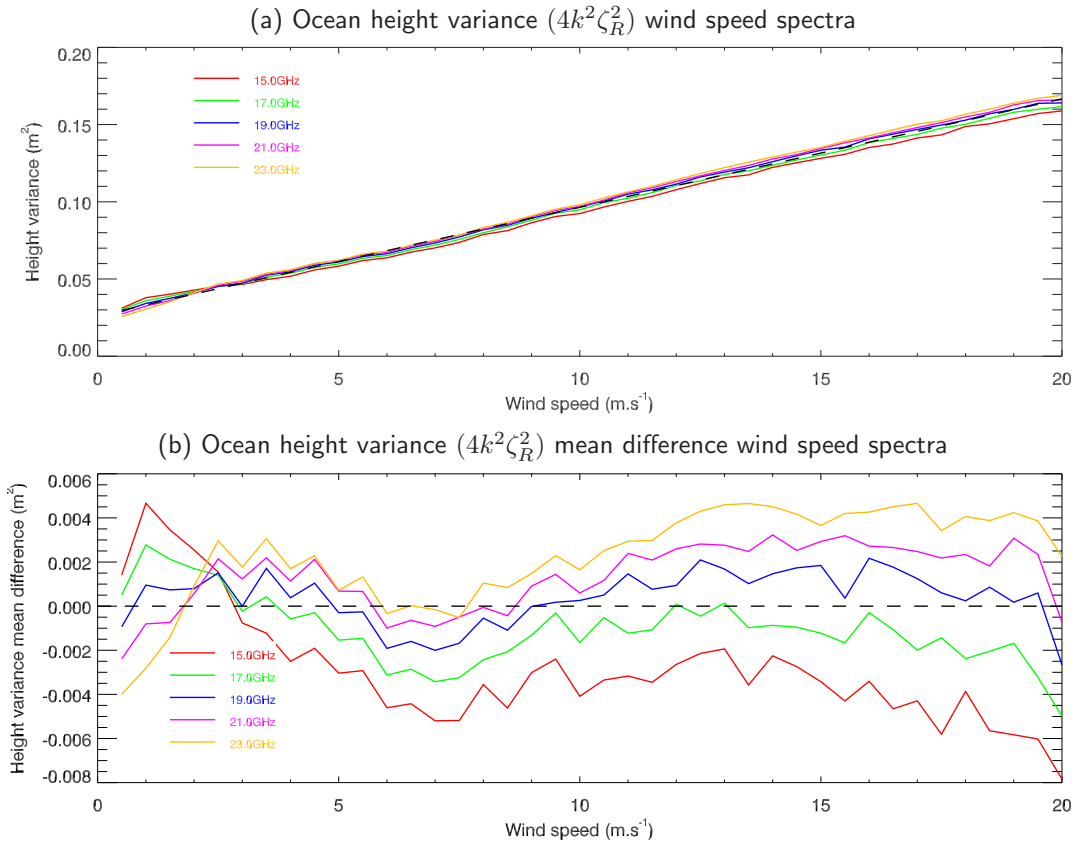


Figure 4.6: Ocean height variance wind speed spectra used for the small-scale reflectivity correction. **(a)** Actual height variance spectra in the LUT. Dashed black line is the linear fit to the average for all frequencies. **(b)** Height variance mean difference spectra obtained by subtracted the mean value and slope from the data, highlighting the noisiness in the LUT data.

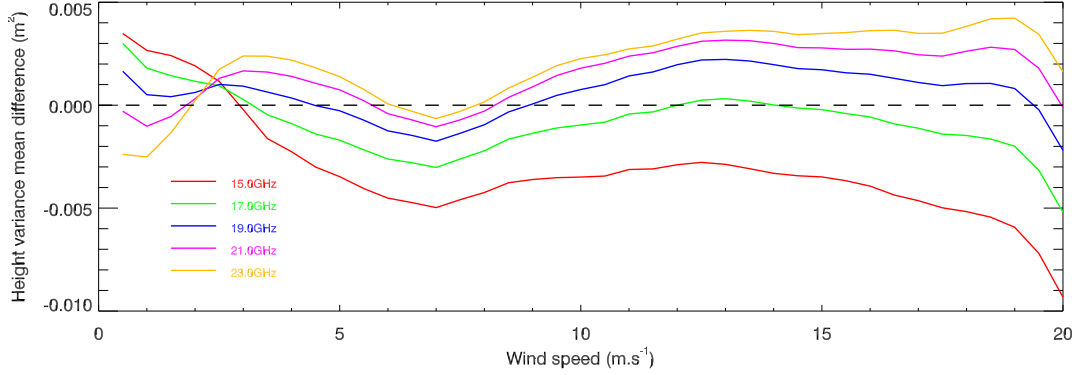


Figure 4.7: Ocean height variance mean difference spectra obtained from smoothed data. Original data was smoothed using a Savitzky-Golay filter in both the wind speed and frequency dimensions. Compare with figure 4.6(b).

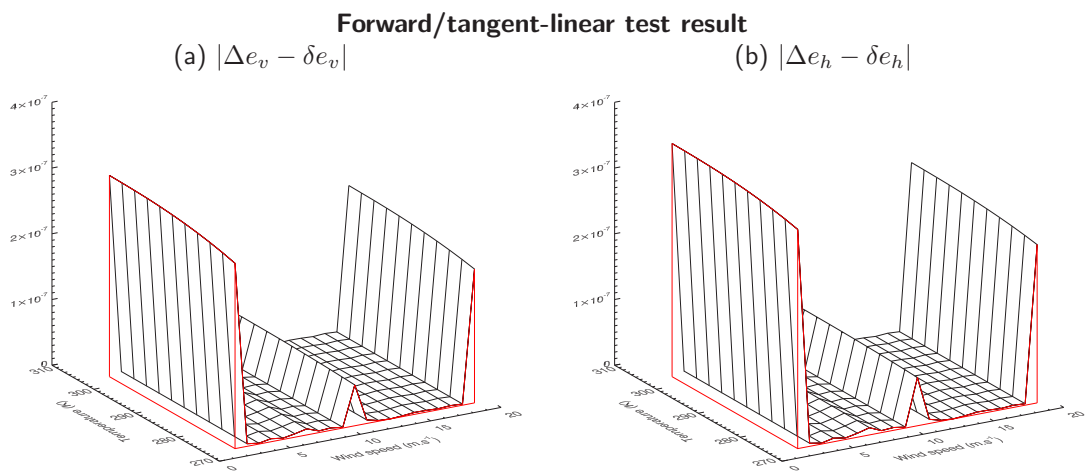
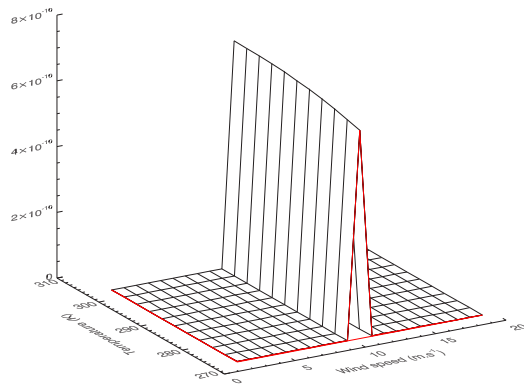


Figure 4.8: Forward/tangent-linear test residuals at 19GHz for $\alpha=0.1$ using the smoothed ocean height variance spectra. Peak residuals are $\sim 2\text{--}10$ times less than those using the original height variance data. **(a)** Vertically polarised test residual (compare with figure 4.4(e)). **(b)** Horizontally polarised test residual (compare with figure 4.4(f)).

Forward/tangent-linear test result

(a) Wind speed test gridpoint at
LUT hinge point of 10ms^{-1}



(b) No wind speed test gridpoint
corresponds with LUT hinge points

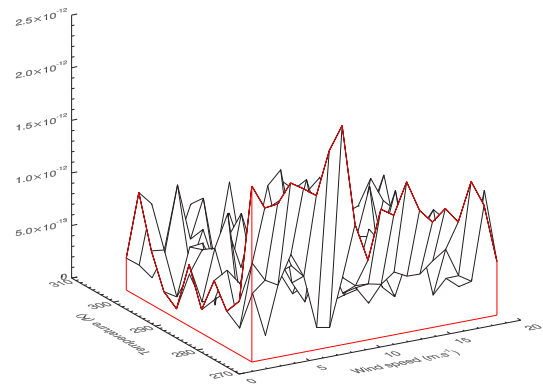


Figure 4.9: Forward/tangent-linear vertically polarised test residuals at 19GHz for $\alpha=0.0001$ for different wind speed grid spacings. Compare with figure 4.5(a). **(a)** Edge wind speed values no longer correspond with LUT hinge points, but centre value at 10ms^{-1} does. **(b)** No wind speed values correspond with LUT hinge points.

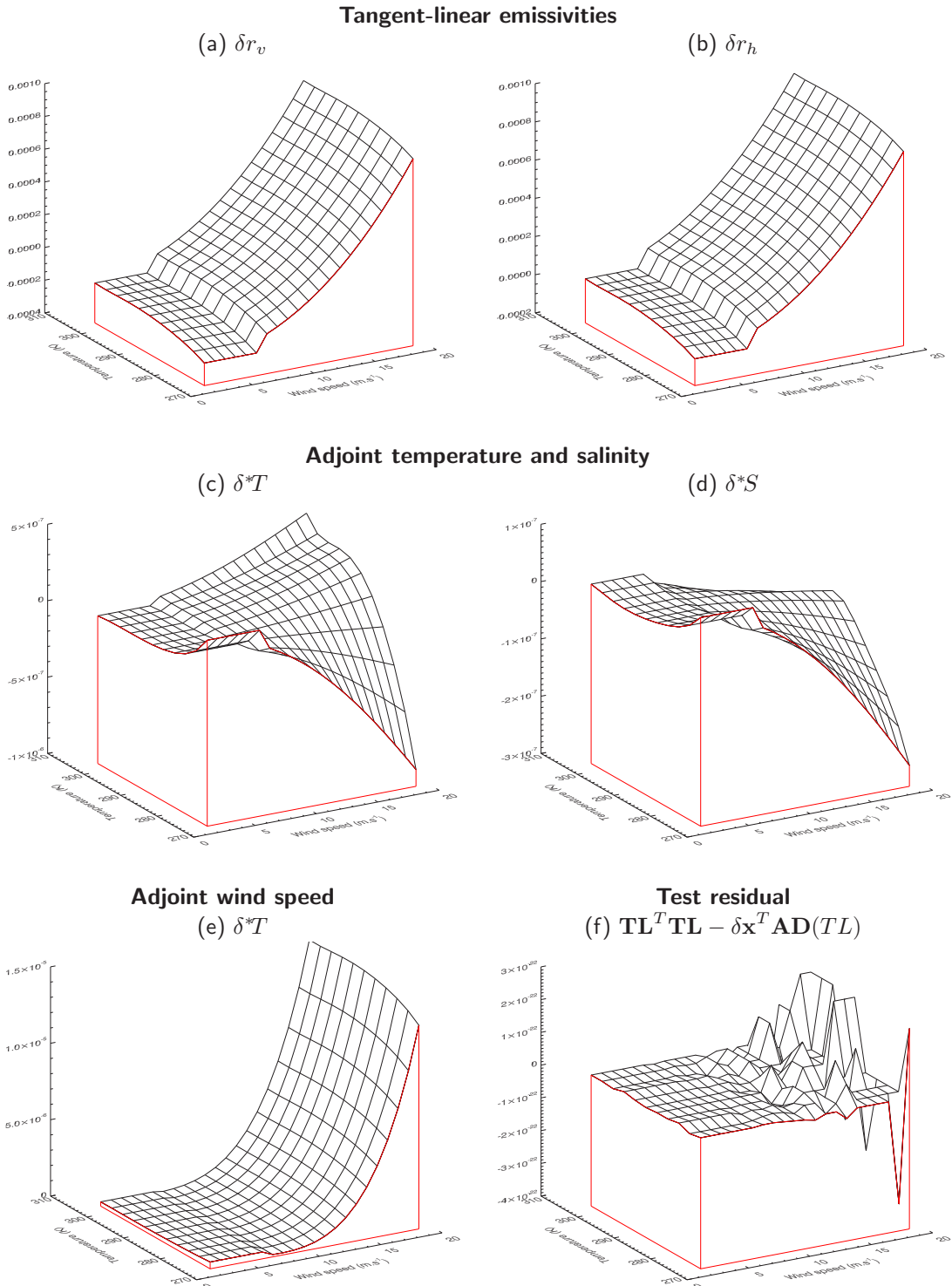


Figure 4.10: Example of quantities used to test the TL/AD routines for δT , δS , and δW inputs of 0.1, a salinity of 35‰, an incidence angle of 30° at a frequency of 7.0GHz. (a) Tangent-linear vertical emissivity. (b) Tangent-linear horizontal emissivity. (c) Adjoint temperature. (d) Adjoint salinity. (e) Adjoint wind speed. (f) Test residual (see eqn.4.1).

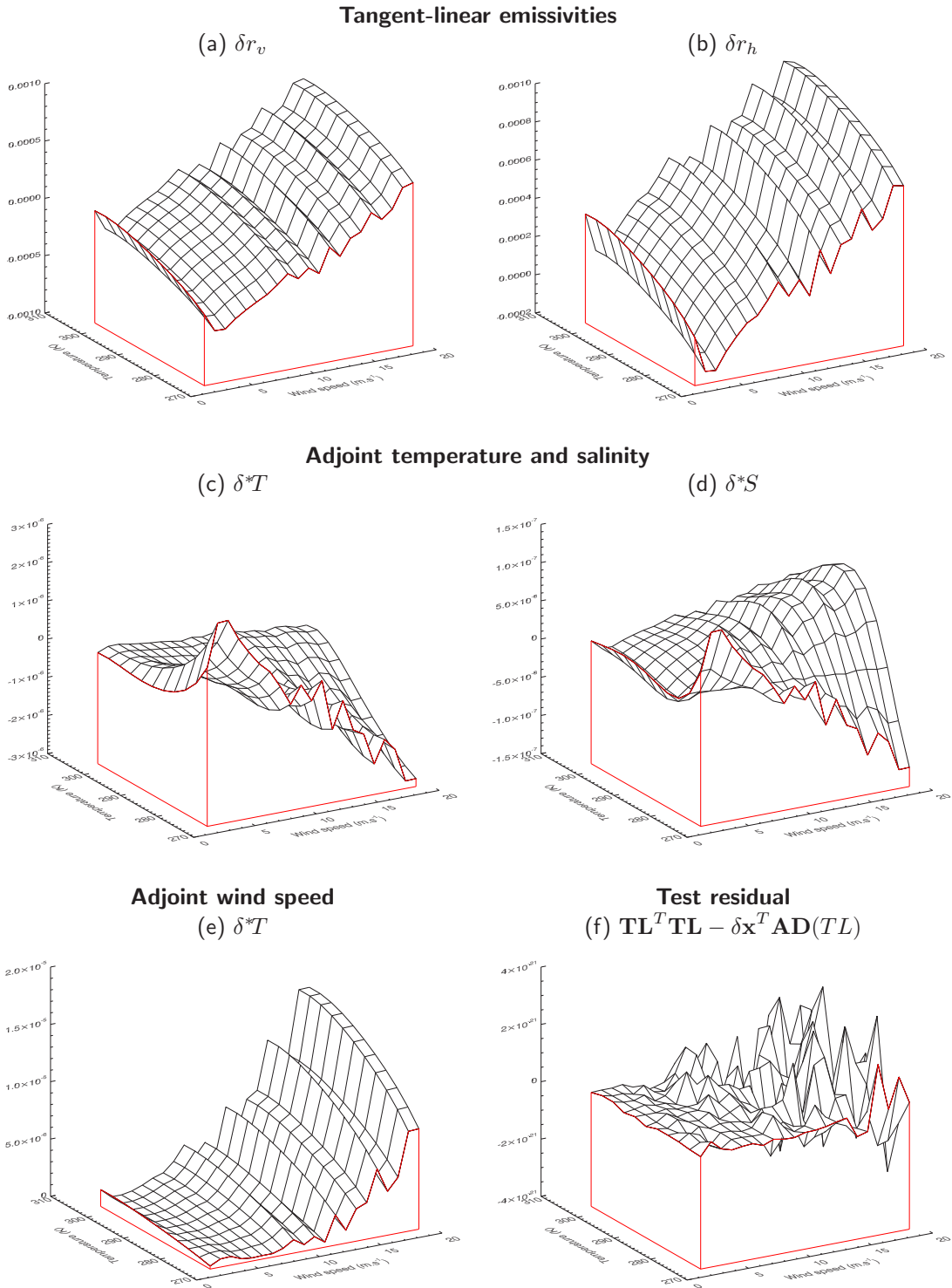


Figure 4.11: Example of quantities used to test the TL/AD routines for δT , δS , and δW inputs of 0.1, a salinity of 35‰, an incidence angle of 30° at a frequency of 19.0GHz. (a) Tangent-linear vertical emissivity. (b) Tangent-linear horizontal emissivity. (c) Adjoint temperature. (d) Adjoint salinity. (e) Adjoint wind speed. (f) Test residual (see eqn.4.1).

5 Comparison of emissivity models in the CRTM

The microwave sea surface emissivity model used in the current CRTM release (v1.1) is Fastem1[[English and Hewison, 1998](#)]. Comparison of this model with the updated LF_MWSSEM model, as well as with Fastem3 (REF!), for the low frequency ($f > 20\text{GHz}$) channels of the Aqua AMSR-E instrument are shown in figure 5.1. The difference between the Fastem1 and new models is very large for the lowest frequency with a $\sim 20\%$ decrease in the computed emissivity at 6.925GHz. The percentage change decreases as the frequency increases with a more modest $\sim 5\%$ decrease at 18.7GHz. The difference between the LF_MWSSEM and Fastem3 models is relatively uniform at $\sim 2\text{-}5\%$ for all frequencies.

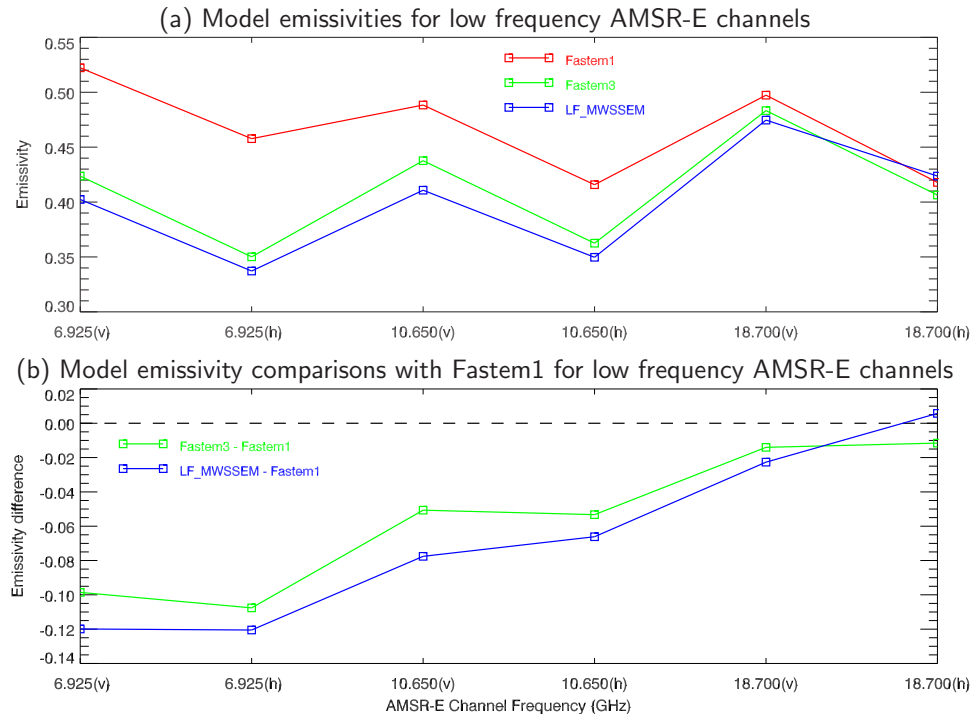


Figure 5.1: Comparison of different emissivity models for the low frequency AMSR-E channels. **(a)** The computed emissivity spectra. Note the large difference between Fastem1 (current CRTM model) and the other models. **(b)** The emissivity spectra differences with respect to Fastem1. The newer models provide a 20% decrease in the computed emissivities at these frequencies.

The impact of these emissivity model changes on computed brightness temperatures was gauged by running the standard CRTM “smoke test”³ using a small set of climatological profiles for a series of microwave instruments: Aqua AMSR-E, NOAA-18 AMSU-A and MHS, and DMSP-16 SSMIS. The average and RMS brightness temperature difference for the LF_MWSSEM-Fastem1 test runs are shown in figure 5.2. As expected, for the lowest frequencies of AMSR-E the temperatures differences are very large at $\sim 30\text{K}$. For the other instrument where the frequencies of the surface sensitive channels are generally greater than 20GHz, the differences are smaller, but still significant in the 1-5K range.

For comparison, the average and RMS brightness temperature difference for the LF_MWSSEM-Fastem3 test runs are shown in figure 5.3. Only for those channels with frequencies less than 20GHz show any impact but the differences are still quite large. Note that the SSMIS channels are not ordered in increasing frequency, hence the ΔT_B spikes for channel 12 and 13 ($f = 19.35\text{GHz}$)

³a simple test to catch large defects but disregard trivial ones.

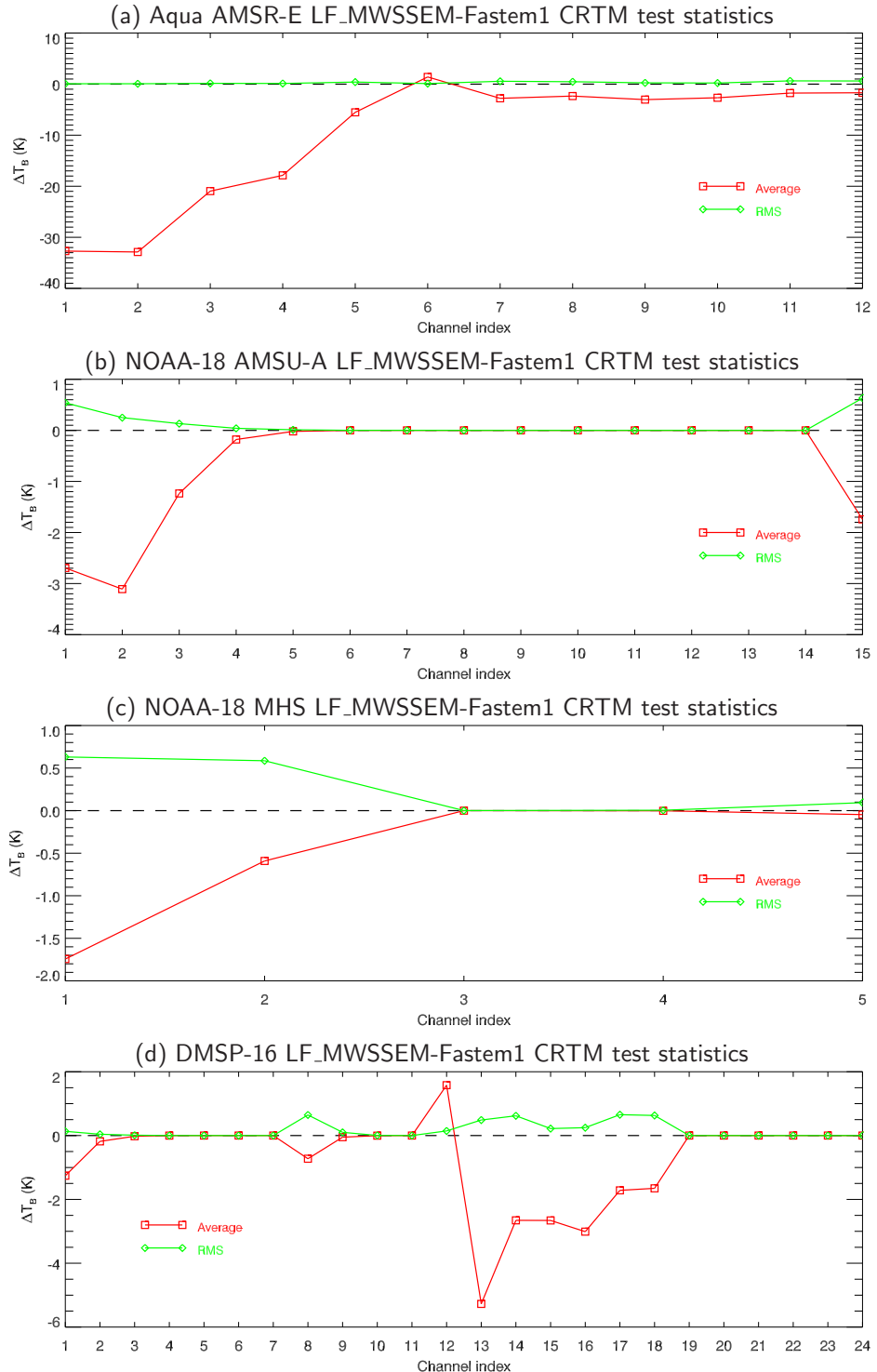


Figure 5.2: CRTM ΔT_B statistics between the LF_MWSSEM and Fastem1 models. **(a)** Aqua AMSR-E. Note that beyond channel 6, $f > 20\text{GHz}$ so the LF_MWSSEM invokes Fastem3. **(b)** NOAA-18 AMSU-A. All AMSU-A channels are $f > 20\text{GHz}$. **(c)** NOAA-18 MHS. Again, all MHS channels are $f > 20\text{GHz}$. **(d)** DMSP-16 SSMIS.

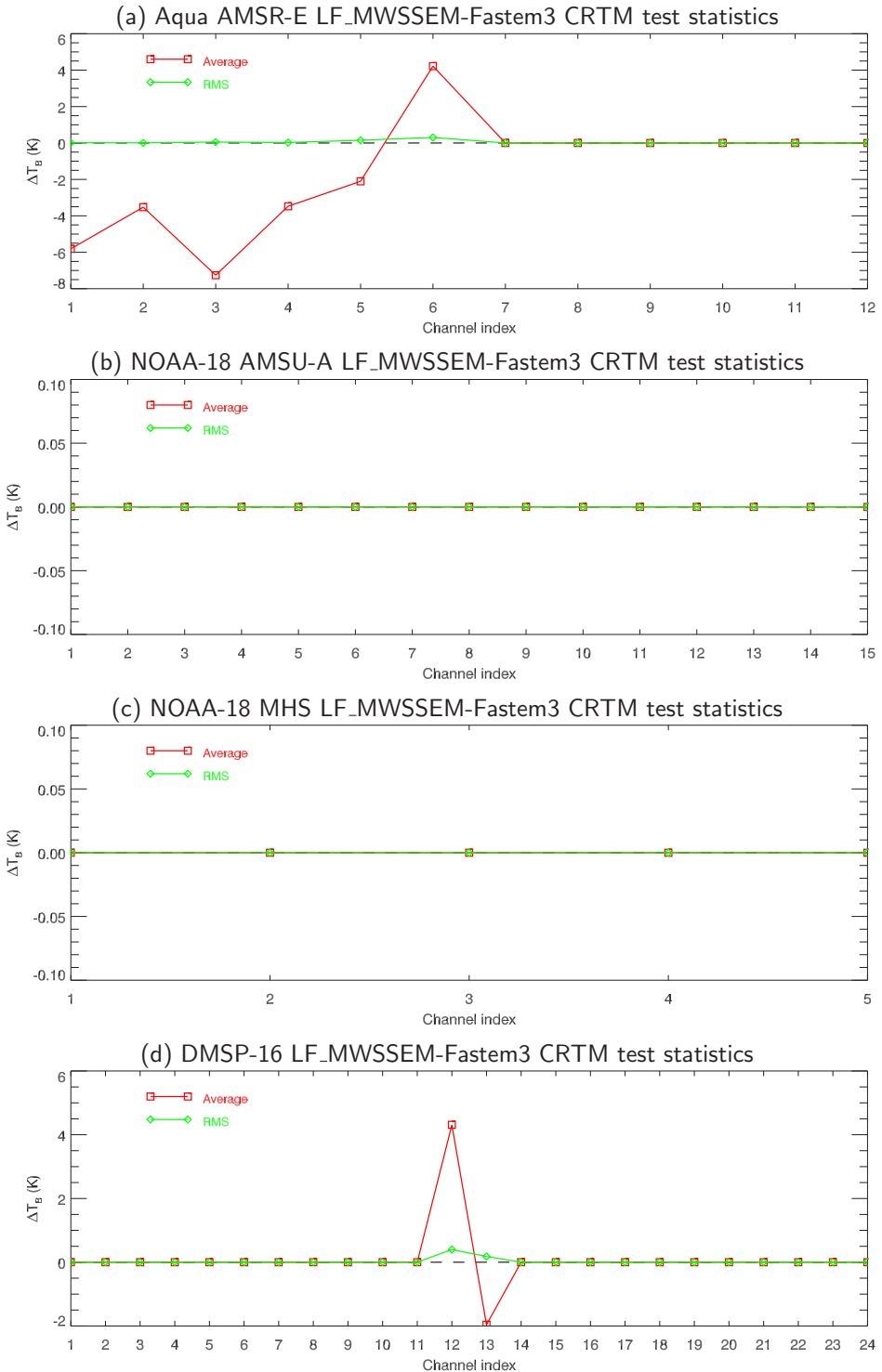


Figure 5.3: CRTM ΔT_B statistics between the LF_MWSSEM and Fastem3 models. Where the LF_MWSSEM invokes Fastem3 (for $f > 20\text{GHz}$), the differences are identically zero. **(a)** Aqua AMSR-E. **(b)** NOAA-18 AMSU-A. **(c)** NOAA-18 MHS. **(d)** DMSP-16 SSMIS. Channels 12 and 13 have $f = 19.35\text{GHz}$.

6 Conclusions

The low frequency microwave sea surface emissivity model has been shown to be internally consistent across its forward, tangent-linear, and adjoint forms.

Validating the forward/tangent-linear model consistency for frequencies greater than 15GHz proved slightly difficult due to the impact that the noisy ocean height variance LUT data had on the resultant emissivities due to the applied small-scale correction. Smoothing the ocean height variance data did decrease the test residuals, but did not eliminate particular features associated with interpolation across LUT hingepoints. Visual inspection of a selection of FWD/TL residuals for various temperatures, salinities, and wind speeds was required to verify the tests. No rigorous objective method was found that could be applied successfully for all combinations of inputs.

Validation of the tangent-linear/adjoint model was comparatively easy in that all test residuals could be objectively compared to within numerical precision. All model components passed this test.

The impact of the updated microwave sea surface emissivity model on computed brightness temperatures in the CRTM can be quite large, 20-30K, for those channels that are sensitive to the surface. The largest portion of the change is due to the emissivity model in the current v1.1 release of the CRTM being Fastem1 which is known to not handle low frequencies very well. However, for the very lowest frequencies tested, the low frequency model still produces an additional brightness temperature difference from Fastem3 of the order of 4-8K.

References

- A.W. Bjerkaas and F.W. Riedel. Proposed model for the elecvation spectrum of a wind-roughened sea surface. Technical Memorandum TG 1328, JHU/APL, December 1979.
- M. Born and E. Wolf. *Principles of Optics*. Cambridge University Press, seventh edition, 1999.
- W.J. Ellison, S.J. English, K. Lamkaouchi, A. Balana, E. Obligis, G. DeBlonde, T.J. Hewison, P. Bauer, G. Kelly, and L. Eymard. A comparison of ocean emissivity models using the Advanced Microwave Sounding Unit, the Special Sensor Microwave Imager, the TRMM Microwave Imager, and airborne radiometer observations. *J. Geophys. Res.*, 108(D21):ACL 1,1–14, 2003.
- S. English and T. Hewison. A fast generic millimeter-wave emissivity model. In *Microwave Remote Sensing of the Atmosphere and Environment*, volume 3503, pages 288–300. SPIE, Sep. 1998. URL <http://dx.doi.org/10.1117/12.319490>.
- C. Guillou, W. Ellison, L. Eymard, K. Lamkaouchi, C. Prigent, G. Delbos, G. Balana, and S. Boukabara. Impact of new permittivity measurements on sea surface emissivity modeling in microwaves. *Radio Sci.*, 33(3):649–667, 1998.
- A. Guissard and P. Sobieski. An approximate model for the microwave brightness temperature of the sea. *Int. J. Remote Sensing*, 8(11):1607–1627, 1987.
- M. Kazumori, Q. Liu, R. Treadon, and J.C. Derber. Impact study of AMSR-E radiances in the NCEP Global Data Assimilation System. *Mon. Wea. Rev.*, 136(2):541–559, 2008.
- W.H. Press, S.A. Teukolsy, W.T. Vetterling, and B.P. Flannery. *Numerical Recipes in Fortran*. Cambridge University Press, second edition, 1992.

A Fresnel Reflectivity Derivation

This section merely derives the Fresnel reflectivity equations used in the CRTM microwave sea surface emissivity from the more typical equations.

As defined in section 1.5.2 in [Born and Wolf \[1999\]](#), the complex amplitudes of the reflected waves parallel (vertical) and perpendicular (horizontal) to the plane of incidence of an air/ocean water interface are given by,

$$R_{\parallel} = \frac{n_2 \cos \theta_i - n_1 \cos \theta_t}{n_2 \cos \theta_i + n_1 \cos \theta_t} \cdot A_{\parallel} \quad (\text{A.1})$$

and

$$R_{\perp} = \frac{n_1 \cos \theta_i - n_2 \cos \theta_t}{n_1 \cos \theta_i + n_2 \cos \theta_t} \cdot A_{\perp} \quad (\text{A.2})$$

where n_1 and n_2 are the refractive indices of air and ocean water respectively, θ_i and θ_t the angles of incidence and transmission respectively, and A represents the complex amplitude of the incident wave. Additionally, the reflectivity is given by the ratio,

$$r = \frac{|R|^2}{|A|^2} \quad (\text{A.3})$$

The refractive index of a medium can be expressed via Maxwell's formula,

$$n = \sqrt{\epsilon \mu}$$

where we can assume the magnetic permeability of ocean water is unity, such that

$$n_2 = \sqrt{\epsilon} \quad (\text{A.4})$$

Setting the refractive index of air to a value of 1.0, we can use equation [A.4](#) in Snell's law to obtain a substitution for $\cos \theta_t$,

$$\begin{aligned} \sqrt{\epsilon} \sin \theta_t &= \sin \theta_i \\ \text{i.e. } \sin^2 \theta_t &= \frac{\sin^2 \theta_i}{\epsilon} \\ \cos^2 \theta_t &= 1 - \frac{1 - \cos^2 \theta_i}{\epsilon} \\ &= \frac{\epsilon - 1 + \cos^2 \theta_i}{\epsilon} \\ \therefore \cos \theta_t &= \sqrt{\frac{\epsilon - 1 + \cos^2 \theta_i}{\epsilon}} \end{aligned} \quad (\text{A.5})$$

Substituting equations [A.4](#) and [A.5](#) into equation [A.1](#) and multiplying by $\sqrt{\epsilon}/\sqrt{\epsilon}$ we get,

$$\begin{aligned} R_{\parallel} &= \frac{\sqrt{\epsilon} \cos \theta_i - \sqrt{\frac{\epsilon - 1 + \cos^2 \theta_i}{\epsilon}} \cdot \sqrt{\epsilon}}{\sqrt{\epsilon} \cos \theta_i + \sqrt{\frac{\epsilon - 1 + \cos^2 \theta_i}{\epsilon}} \cdot \sqrt{\epsilon}} \cdot A_{\parallel} \\ &= \frac{\epsilon \cos \theta_i - \sqrt{\epsilon - 1 + \cos^2 \theta_i}}{\epsilon \cos \theta_i + \sqrt{\epsilon - 1 + \cos^2 \theta_i}} \cdot A_{\parallel} \end{aligned} \quad (\text{A.6})$$

with the reflectivity given by equation [A.3](#)

$$r_{\parallel} = \left| \frac{\epsilon \cos \theta_i - \sqrt{\epsilon - 1 + \cos^2 \theta_i}}{\epsilon \cos \theta_i + \sqrt{\epsilon - 1 + \cos^2 \theta_i}} \right|^2 \quad (\text{A.7})$$

Similarly for the equation A.2,

$$\begin{aligned}
R_{\perp} &= \frac{\cos \theta_i - \sqrt{\epsilon} \sqrt{\frac{\epsilon - 1 + \cos^2 \theta_i}{\epsilon}}}{\cos \theta_i + \sqrt{\epsilon} \sqrt{\frac{\epsilon - 1 + \cos^2 \theta_i}{\epsilon}}} \cdot A_{\perp} \\
&= \frac{\cos \theta_i - \sqrt{\epsilon - 1 + \cos^2 \theta_i}}{\cos \theta_i + \sqrt{\epsilon - 1 + \cos^2 \theta_i}} \cdot A_{\perp}
\end{aligned} \tag{A.8}$$

with reflectivity,

$$r_{\perp} = \left| \frac{\cos \theta_i - \sqrt{\epsilon - 1 + \cos^2 \theta_i}}{\cos \theta_i + \sqrt{\epsilon - 1 + \cos^2 \theta_i}} \right|^2 \tag{A.9}$$

B Impact on computational speed due to polynomial calculations

Both the [Ellison et al. \[2003\]](#) and [Guillou et al. \[1998\]](#) emissivity models use polynomial fits to data to represent various components of the complex ocean surface permittivity. Forward, tangent-linear, and adjoint polynomial computation routines were written to simplify their evaluation.

The permittivity codes were profiled with the polynomial calculations performed inline, and using the polynomial routines with the profiler outputs. The results are shown in figures [B.1](#) and [B.2](#) for the Ellison code, and figures [B.3](#) and [B.4](#) for the Guillou code. On average, the inline polynomial evaluation results in the test code running approximately two (Ellison) to three (Guillou) times faster than if evaluation routines were used. The larger impact for the Guillou code is likely due to there being more polynomials to evaluate, many with six coefficients.

Note that the 2-3 \times factor from the profiling tests does not necessarily translate into wall-clock time.

```
Each sample counts as 0.01 seconds.
% cumulative self
time   seconds   seconds   calls  name
31.43    2.36    2.36        1  MAIN__
22.17    4.03    1.67  16669800  unit_test_MOD_fp_equal_within_scalar
21.97    5.68    1.65  9724050  ocean_permittivity_MOD_ellison_ocean_permittivity
19.04    7.11    1.43  9261000  ocean_permittivity_MOD_ellison_ocean_permittivity_tl
  3.46    7.37    0.26  1852200  ocean_permittivity_MOD_ellison_ocean_permittivity_ad
  0.87    7.43    0.07  16669800  unit_test_MOD_last_test_failed
  0.73    7.49    0.06  16669800  unit_test_MOD_test_passed
  0.33    7.51    0.03          unit_test_MOD_fp_equal_within_rank1
```

Figure B.1: Profile results for Ellison permittivity tests with polynomial evaluation performed inline.

```
Each sample counts as 0.01 seconds.
% cumulative self
time   seconds   seconds   calls  name
28.67    4.09    4.09  38896200  ocean_permittivity_MOD_poly
18.28    6.69    2.61  37044000  ocean_permittivity_MOD_poly_tl
14.11    8.70    2.01        1  MAIN__
12.32   10.46    1.76  9724050  ocean_permittivity_MOD_ellison_ocean_permittivity
10.77   11.99    1.54  16669800  unit_test_MOD_fp_equal_within_scalar
  8.00   13.13    1.14  9261000  ocean_permittivity_MOD_ellison_ocean_permittivity_tl
  3.47   13.63    0.50  7408800  ocean_permittivity_MOD_poly_ad
  2.84   14.03    0.41  1852200  ocean_permittivity_MOD_ellison_ocean_permittivity_ad
  0.84   14.15    0.12  16669800  unit_test_MOD_test_passed
  0.56   14.23    0.08  16669800  unit_test_MOD_last_test_failed
  0.07   14.24    0.01          unit_test_MOD_test_failed
  0.04   14.25    0.01          1  timing_utility_MOD_begin_timing
```

Figure B.2: Profile results for Ellison permittivity tests using polynomial evaluation subroutines

```

Each sample counts as 0.01 seconds.
% cumulative      self
time   seconds    seconds    calls  name
25.66    2.15     2.15        1  MAIN_-
24.94    4.24     2.09  9261000 ocean_permittivity_MOD_guillou_ocean_permittivity_tl
24.46    6.29     2.05  9724050 ocean_permittivity_MOD_guillou_ocean_permittivity
16.77    7.70     1.41 16669800 unit_test_MOD_fp_equal_within_scalar
 5.01    8.12     0.42 1852200 ocean_permittivity_MOD_guillou_ocean_permittivity_ad
 2.09    8.29     0.18 16669800 unit_test_MOD_test_passed
 0.90    8.37     0.08 14817600 unit_test_MOD_last_test_failed
 0.12    8.38     0.01           unit_test_MOD_test_failed

```

Figure B.3: Profile results for Guillou permittivity tests with polynomial evaluation performed inline.

```

Each sample counts as 0.01 seconds.
% cumulative      self
time   seconds    seconds    calls  name
38.64    9.85     9.85  68068350 ocean_permittivity_MOD_poly
21.76   15.39     5.55  64827000 ocean_permittivity_MOD_poly_tl
 9.50   17.81     2.42  9724051 ocean_permittivity_MOD_guillou_ocean_permittivity
 9.34   20.19     2.38           MAIN_-
 7.10   22.00     1.81 16669800 unit_test_MOD_fp_equal_within_scalar
 5.89   23.50     1.50  9261000 ocean_permittivity_MOD_guillou_ocean_permittivity_tl
 5.30   24.85     1.35 12965400 ocean_permittivity_MOD_poly_ad
 1.37   25.20     0.35 1852200 ocean_permittivity_MOD_guillou_ocean_permittivity_ad
 0.47   25.32     0.12 16669800 unit_test_MOD_test_passed
 0.31   25.40     0.08 14817600 unit_test_MOD_last_test_failed
 0.12   25.43     0.03           unit_test_MOD_fp_equal_within_rank1
 0.12   25.46     0.03           unit_test_MOD_test_failed
 0.08   25.48     0.02           ocean_permittivity_MOD_ellison_ocean_permittivity_ad

```

Figure B.4: Profile results for Guillou permittivity tests using polynomial evaluation subroutines